

CZECH TECHNICAL UNIVERSITY  
FACULTY OF NUCLEAR SCIENCES AND PHYSICAL ENGINEERING  
DEPARTMENT OF PHYSICS

# Measurement of double beta decay of $^{116}\text{Cd}$ in the NEMO3 experiment

RESEARCH WORK

Author: **Jiří Bočan**  
Supervisor: **Ing. Ivan Štekl, CSc.**  
Consultants: **Ing. Ladislav Vála, PhD, Laurent Simard, PhD**  
School year: **2003/2004**



# Acknowledgement

Firstly, I would like to thank Serge Jullian, the spokesman of the NEMO Collaboration, who officially admitted me into the NEMO Collaboration.

Next, my great thanks belong to Ivan Štekl from the Institute of Experimental and Applied Physics, Czech Technical University (IEAP CTU) in Prague, for introducing me into the NEMO Collaboration and also for his big support and help.

I would like to express my high gratitude to Ladislav Vála also from the IEAP CTU for his leading and teaching me everything about the analysis of data from NEMO experiment, for his advice, and as well as for his attentive reading and English correction of this work.

My thanks also go to Laurent Simard from LAL Orsay for helping me with programming and for the useful consultations.

Finally, the biggest thanks and my highest gratitude are dedicated to my parents for their full support, encouragement and understanding.

Thank you!



# Contents

<b>Introduction</b>	<b>1</b>
<b>1 Double beta decay of <math>^{116}\text{Cd}</math></b>	<b>3</b>
1.1 Double beta decay . . . . .	3
1.2 Methods of double beta decay measurement . . . . .	4
1.3 Isotope $^{116}\text{Cd}$ . . . . .	6
<b>2 NEMO experiment</b>	<b>8</b>
2.1 Research and development prototypes . . . . .	8
2.1.1 NEMO1 . . . . .	8
2.1.2 NEMO2 . . . . .	8
2.2 NEMO3 experiment . . . . .	9
2.2.1 General description . . . . .	10
2.2.2 Tracking wire chamber . . . . .	10
2.2.3 Calorimeter . . . . .	11
2.2.4 NEMO3 sources . . . . .	13
2.2.5 Reduction of external backgrounds . . . . .	14
2.2.6 Trigger . . . . .	15
2.2.7 Data acquisition system and detector monitoring . . . . .	16
2.3 NEMO3 background . . . . .	16
2.3.1 Background of the experiment . . . . .	16
2.3.2 Internal background . . . . .	16
2.3.3 External background . . . . .	17
2.3.4 Radon and thoron . . . . .	17
2.3.5 Neutrons . . . . .	18
2.3.6 Photons from laboratory surrounding and cosmic rays . . . . .	18
2.3.7 Detector radiopurity . . . . .	19
<b>3 Monte-Carlo simulations</b>	<b>20</b>
3.1 Software tools . . . . .	20
3.2 Trigger for Monte-Carlo simulations . . . . .	20
3.3 Types of simulated events . . . . .	21
3.4 Definition of particles in Monte-Carlo events . . . . .	21
3.4.1 Electrons . . . . .	21
3.4.2 $\alpha$ -particles . . . . .	22
3.5 Construction of selection criteria . . . . .	22
3.5.1 Topological and time-of-flight cuts . . . . .	23
3.5.2 Electron energy cuts . . . . .	24
3.5.3 Angle between the emitted electrons . . . . .	25
3.6 Final set of the cuts for two-electron search . . . . .	26

<b>4 Data analysis</b>	<b>31</b>
4.1 Software tools for the data analysis . . . . .	31
4.2 Analyzed runs . . . . .	32
<b>Conclusion</b>	<b>35</b>
<b>References</b>	<b>37</b>

# List of Figures

1.1	Simplified Feynman diagrams of the $2\nu\beta\beta$ and $0\nu\beta\beta$ decays. . . . .	5
1.2	The $\beta\beta$ decay spectrum. . . . .	5
1.3	The $\beta\beta$ decay scheme of $^{116}\text{Cd}$ . . . . .	7
2.1	The NEMO1 prototype scheme. . . . .	8
2.2	The NEMO2 prototype scheme. . . . .	9
2.3	Schematic view of the NEMO3 detector core without external shielding. . . . .	10
2.4	The NEMO3 tracking device. . . . .	11
2.5	The scheme of one NEMO3 sector. . . . .	12
2.6	The NEMO3 source arrangement. . . . .	14
2.7	The shield of NEMO3 detector. . . . .	15
2.8	Internal background processes generating two-electron events. . . . .	17
2.9	External background processes generating two-electron events. . . . .	17
2.10	The $^{238}\text{U}$ and $^{232}\text{Th}$ decay chains. . . . .	18
3.1	The possible scenarios of the two-electron events. . . . .	22
3.2	The examples of the $\beta\beta$ decay events. . . . .	22
3.3	The examples of the $\beta\beta$ decay events with $\alpha$ -particle. . . . .	23
3.4	The single-electron energy spectrum for simulated events from $^{116}\text{Cd}$ . . . . .	24
3.5	The single-electron energy spectra for simulated isotopes. . . . .	28
3.6	The total two-electron energy spectra for simulated isotopes. . . . .	29
3.7	Angular distribution of the two emitted electrons for different simulated isotopes. . . . .	30

# List of Tables

1.1	The $2\nu\beta\beta$ decay nuclides. . . . .	4
1.2	The basic nuclear characteristics of $^{116}\text{Cd}$ . . . . .	7
1.3	Experimentally determined $\beta\beta$ decay half-lives of $^{116}\text{Cd}$ . . . . .	7
2.1	The NEMO2 results. . . . .	9
2.2	Total radioactivity of NEMO3 Hamamatsu Photomultipliers. . . . .	12
2.3	Characteristics of the source foils of the NEMO3 sectors. . . . .	13
2.4	The radioactivity limits for impurities in the NEMO3 Cd source. . . . .	14
2.5	Radioactivity measurements of the NEMO3 source foils. . . . .	19
2.6	Total radioactivity for the main NEMO3 detector components. . . . .	19
3.1	List of simulated types of events. . . . .	21
3.2	The simulated isotope characteristics. . . . .	23
3.3	S/B ratios together with expected number of signal events after 1 year for different limits on $E_{min}$ and $E_{max}$ . . . . .	25
3.4	S/B ratios together with expected number of signal events after 1 year for different limits on $E_{tot}$ . . . . .	25
3.5	The influence of energy cuts on the number of selected events. . . . .	26
3.6	The optimal electron emission angle estimation. . . . .	26
3.7	The influence of angle cut on the number of selected events. . . . .	27
4.1	Summary of analysed runs. . . . .	32
4.2	The number of selected events for each month. . . . .	32
4.3	The expected number of background events determined from MC simulations for the considered acquisition period. . . . .	33

# Introduction

Double beta decay is a rare process which was predicted in the thirties of the 20th century (two-neutrino double beta decay - M. Goeppert Mayer, 1935; neutrinoless double beta decay - W. H. Furry, 1939). In spite of the fact that there are many nuclei liable to this process, there are only several isotopes, which are suitable for experimental observation.

This research work is dedicated to the measurement of the double beta decay of  $^{116}\text{Cd}$  in the NEMO3 experiment. This experiment, located at the Fréjus Underground Laboratory (Modane, France), in which physicists from 15 laboratories from 7 countries participate, examines several isotopes. The greatest effort is concentrated to neutrinoless double beta decay of  $^{100}\text{Mo}$  and  $^{82}\text{Se}$ , but  $^{116}\text{Cd}$  decay can be studied, too.

In the work, only the two-neutrino double beta decay (g.s.  $\rightarrow$  g.s. transition) of  $^{116}\text{Cd}$  will be studied and measured. There are some reasons why the observation of the other processes in cadmium is not possible at present. One of them is a small mass of  $^{116}\text{Cd}$  installed in the detector. Another reason is, that NEMO3 started to collect data only in the February 2003 and, thus, the statistics is still low. Finally, there is quite high level of background caused by radon which complicate a little the signal analysis.

The whole text is divided into four chapters. The first chapter treats in general the double beta decay, the possible ways of its measurement and also presents the isotope  $^{116}\text{Cd}$ . Next chapter is concerned with the NEMO experiment description. Both the technological prototypes - NEMO1 and NEMO2 - are shortly mentioned, but the main part deals with the NEMO3 detector. The principle of operation, the main parts - tracking wire chamber, calorimeter, double beta decay sources, background, shielding - of NEMO3 are described in details.

The last two chapters concentrate to data analysis. The third chapter depicts Monte-Carlo simulations, an important part of analysis, together with construction and definition of the selection criteria, which will be applied on the  $^{116}\text{Cd}$  data during data processing. Finally, the last chapter summarize the results of the analysis.



# Chapter 1

## Double beta decay of $^{116}\text{Cd}$

### 1.1 Double beta decay

Double beta decay ( $\beta\beta$ ) is a rare inner-nucleon process appearing when the ordinary single  $\beta$  decay is energetically forbidden or strongly suppressed by a large angular momentum difference between the initial and final nuclear states.  $\beta\beta$  decay is a process of the second order of Fermi's  $\beta$  decay theory and represents a conversion of a nucleus  $A(Z, N)$  into an isobar with the electric charge differing by two units. At a fundamental level,  $\beta\beta$  decay is a transition of two  $d$  quarks into two  $u$  quarks or vice versa. It occurs in the case of nuclei with even number of protons and also even number of neutrons (even-even nuclei). The corresponding decay rates are very low; a typical lifetime of the nuclei liable to  $\beta\beta$  decay is  $\tau \gtrsim 10^{18}$  years. A typical energy release  $Q_{\beta\beta}$  for  $\beta\beta$  decay is about several MeV [1, 2, 3, 4, 5, 6, 7, 8].

Generally, there are two modes of this decay - two-neutrino double beta decay ( $2\nu\beta\beta$ ) which was firstly theoretically predicted by Goeppert-Mayer in 1935 [9], and the neutrinoless ( $0\nu\beta\beta$ ) double beta decay introduced by Furry in 1939 [10].

The  $2\nu\beta\beta$  process (Figure 1.1-left) conserve electric charge and lepton number, and is permitted in the Standard Model (SM) of particle physics. It implies that neutrinos are the Dirac particles meaning among others the nonequivalence of neutrino and its antiparticle [6, 8]. The basic  $2\nu\beta\beta$  modes are two-electron emission ( $\beta^-\beta^-$ , eq. 1.1), two-positron emission ( $\beta^+\beta^+$ , eq. 1.2), electron capture with emission of positron ( $\beta^+/EC$ , eq. 1.3) and two-electron capture ( $EC/EC$ , eq. 1.4).

$$A(Z, N) \rightarrow A(Z + 2, N - 2) + 2e^- + 2\bar{\nu}_e \quad (1.1)$$

$$A(Z, N) \rightarrow A(Z - 2, N + 2) + 2e^+ + 2\nu_e \quad (1.2)$$

$$e^- + A(Z, N) \rightarrow A(Z - 2, N + 2) + e^+ + 2\nu_e \quad (1.3)$$

$$2e^- + A(Z, N) \rightarrow A(Z - 2, N + 2) + 2\nu_e \quad (1.4)$$

The  $\beta^+\beta^+$  decays are energetically possible only for six nuclei. They are always accompanied by  $EC/EC$  or  $\beta^+/EC$  processes and their rates are much smaller in comparison with the  $\beta^-\beta^-$  processes due to smaller phase space. The predicted  $\beta^+\beta^+$  decay half-lives are of the order of  $10^{25} - 10^{26}$  years, whereas in the case of  $\beta^+/EC$  only about  $10^{22}$  years; for  $EC/EC$  it is on the level of  $10^{20}$  years. Thus, it gives more chance to observe  $EC/EC$  or  $\beta^+/EC$  channels. Nevertheless, up to now, main experimental effort has been concentrated to  $\beta^-\beta^-$  processes (several  $\beta^-\beta^-$  nuclides are listed in Table 1.1).

The  $0\nu\beta\beta$  process (Figure 1.1-right) which is given by:

$$A(Z, N) \rightarrow A(Z \pm 2, N \mp 2) + 2e^\mp, \quad (1.5)$$

is intensively searched for. In this case, neutrino or antineutrino virtually emitted in one of the elementary  $\beta$  decay vertex is absorbed in the other one. It leads to violation of lepton number and chirality. This type of decay is forbidden in SM, however, some exotic models with possible additional

Isotope	$Q_{\beta\beta}$ (keV)	$T_{1/2}^{2\nu\beta\beta}$ (yr)	$A_N$ (%)
$^{146}\text{Nd} \rightarrow ^{146}\text{Sm}$	56±5	–	17.19
$^{98}\text{Mo} \rightarrow ^{98}\text{Ru}$	112±7	–	24.13
$^{80}\text{Se} \rightarrow ^{80}\text{Kr}$	130±9	–	49.61
$^{122}\text{Sn} \rightarrow ^{122}\text{Te}$	364±4	–	4.63
$^{204}\text{Hg} \rightarrow ^{204}\text{Pb}$	416±2	–	6.87
$^{192}\text{Os} \rightarrow ^{192}\text{Pt}$	417±4	–	41.00
$^{186}\text{W} \rightarrow ^{186}\text{Os}$	490±2	–	28.60
$^{114}\text{Cd} \rightarrow ^{114}\text{Sn}$	534±4	–	28.73
$^{170}\text{Er} \rightarrow ^{170}\text{Yd}$	654±2	–	14.90
$^{134}\text{Xe} \rightarrow ^{134}\text{Ba}$	847±10	–	10.40
$^{232}\text{Th} \rightarrow ^{232}\text{U}$	858±6	–	100.00
$^{128}\text{Te} \rightarrow ^{128}\text{Xe}$	868±4	$(2.50 \pm 0.40) \times 10^{24}$	31.69
$^{46}\text{Ca} \rightarrow ^{46}\text{Ti}$	987±4	–	0.004
$^{70}\text{Zn} \rightarrow ^{70}\text{Ge}$	1001±3	–	0.60
$^{198}\text{Pt} \rightarrow ^{198}\text{Hg}$	1048±4	–	7.20
$^{176}\text{Yb} \rightarrow ^{176}\text{Hf}$	1079±3	–	12.70
$^{238}\text{U} \rightarrow ^{238}\text{Pu}$	1145±2	$(2.00 \pm 0.60) \times 10^{21}$	99.27
$^{94}\text{Zr} \rightarrow ^{94}\text{Mo}$	1145±2	–	17.38
$^{154}\text{Sm} \rightarrow ^{154}\text{Gd}$	1252±2	–	22.70
$^{86}\text{Kr} \rightarrow ^{86}\text{Sr}$	1256±5	–	17.30
$^{104}\text{Ru} \rightarrow ^{104}\text{Pd}$	1299±4	–	18.70
$^{142}\text{Ce} \rightarrow ^{142}\text{Nd}$	1418±3	–	11.08
$^{160}\text{Gd} \rightarrow ^{160}\text{Dy}$	1729±1	–	21.86
$^{148}\text{Nd} \rightarrow ^{148}\text{Sm}$	1928±2	–	5.76
$^{110}\text{Pd} \rightarrow ^{110}\text{Cd}$	2013±19	–	11.72
$^{76}\text{Ge} \rightarrow ^{76}\text{Se}$	2040±1	$1.43^{+0.09}_{-0.07} \times 10^{21}$	7.44
$^{124}\text{Sn} \rightarrow ^{124}\text{Te}$	2288±2	–	5.79
$^{136}\text{Xe} \rightarrow ^{136}\text{Ba}$	2479±8	–	8.90
$^{130}\text{Te} \rightarrow ^{130}\text{Xe}$	2533±4	$(0.90 \pm 0.15) \times 10^{11}$	33.80
$^{116}\text{Cd} \rightarrow ^{116}\text{Sn}$	2802±4	$3.30^{+0.40}_{-0.30} \times 10^{19}$	7.49
$^{82}\text{Se} \rightarrow ^{82}\text{Kr}$	2995±6	$(0.90 \pm 0.10) \times 10^{20}$	8.73
$^{100}\text{Mo} \rightarrow ^{100}\text{Ru}$	3034±6	$(8.00 \pm 0.70) \times 10^{18}$	9.63
$^{96}\text{Zr} \rightarrow ^{96}\text{Mo}$	3350±3	$2.10^{+0.80}_{-0.40} \times 10^{19}$	2.80
$^{150}\text{Nd} \rightarrow ^{150}\text{Sm}$	3667±2	$(7.00 \pm 1.70) \times 10^{18}$	5.64
$^{48}\text{Ca} \rightarrow ^{48}\text{Ti}$	4271±4	$4.20^{+2.10}_{-1.00} \times 10^{19}$	0.19

Table 1.1: The  $2\nu\beta\beta$  decay nuclides. For each isotope,  $Q_{\beta\beta}$  value, measured half-life  $T_{1/2}^{2\nu\beta\beta}$  and natural abundance  $A_N$  is listed. Ref. [1, 11, 12].

hypothetical particles allow it. The  $0\nu\beta\beta$  decay implies that neutrinos are of Majorana type (neutrino and antineutrino are identical particles) and new theories beyond Standard Model, which will explain also the neutrino mass, are needed [6, 8].

Two-electron energy spectra of  $2\nu\beta\beta$  and  $0\nu\beta\beta$  modes are shown in Figure 1.2. In the case of the  $2\nu\beta\beta$ , the spectrum is continuous because certain portion of energy is carried out by neutrinos which are not detected while for  $0\nu\beta\beta$ , there is only a peak at  $Q_{\beta\beta}$  value.

## 1.2 Methods of double beta decay measurement

The main common principle of measurement of all the different double beta decay modes is based on detection of electrons, positrons, and annihilation or deexcitation photons. Generally,  $2\nu\beta\beta$  decay half-lives are at the order of  $10^{18} - 10^{26}$  years, thus, to achieve good experimental results, the precise low-level

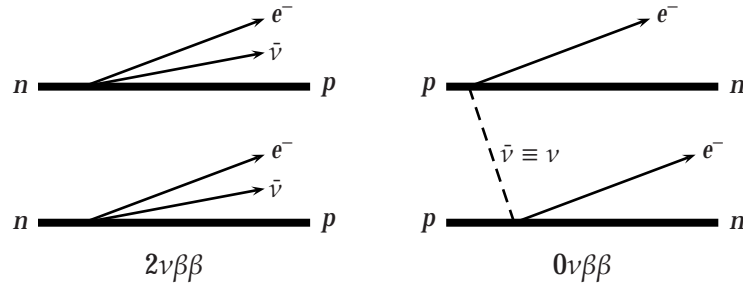


Figure 1.1: Simplified Feynman diagrams of the  $2\nu\beta\beta$  and  $0\nu\beta\beta$  decays.

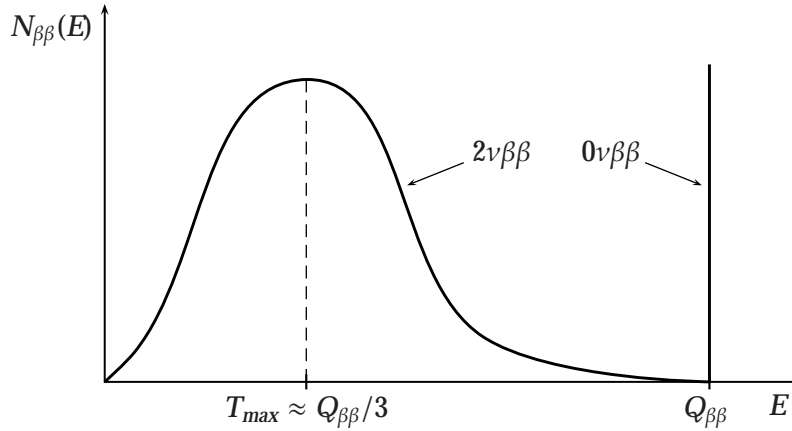


Figure 1.2: The  $\beta\beta$  decay spectrum.

counting techniques are required. For such measurement, highly isotopic enriched materials with high  $Q_{\beta\beta}$  value (Table 1.1) and very low background techniques are needed.

The main background sources are cosmic-ray muons, the man-made  $^{137}\text{Cs}$ , the products of natural decay chains of U and Th, the cosmogenic produced unstable isotopes within the detector components, neutrons,  $^{222}\text{Rn}$  and  $^{40}\text{K}$ . All these influences should be reduced by building the experiments deeply underground, using pure materials for a detector set-up design, minimizing their exposure to cosmic rays and shielding them by low-active materials. Radon and its daughters can be well-suppressed by working either in a pure nitrogen (air-free) atmosphere or by a possibility of air-cleaner installation and by placing the detector into the air-tight box.

In general, the  $\beta\beta$  experiments can be divided into two groups - calorimeters (Ge detectors, bolometers<sup>1</sup>) which measure only the released energy with very good accuracy, and tracking detectors which provide more details about events, for example tracking information, while energy is measured from track curvature (time projection chambers, TPC) or with calorimeters (NEMO, ELEGANT).

Another possibility is to divide these experiments regarding whether they use active or passive  $\beta\beta$  sources. The former use the same material as  $\beta\beta$  source and detector (for example  $^{76}\text{Ge}$ ) but they only can measure the sum energy of both electrons. The latter use different materials but they can provide more information like measurement of the energy and tracks, separately [8].

**Geochemical experiments** investigate the very old ores which accumulated a significant amount of the daughter nuclei. The advantage of these experiments is the long exposition time of up to  $10^9$  years. But thanks to the problems with the determination of the accurate age of ore, excluding the

<sup>1</sup>bolometer = apparatus for the radiant heat measurement

other processes producing the daughters, avoiding a high initial concentration of the daughters and having the significant source strength, only  $^{82}\text{Se}$  and  $^{130}\text{Te}$  are usable. The detection is based on the isotopic anomalies due to  $\beta\beta$  decay ( $^{82}\text{Se} \rightarrow ^{82}\text{Kr}$ ,  $^{128,130}\text{Te} \rightarrow ^{128,130}\text{Xe}$ ) which are measured by mass spectrometry.

**Radiochemical experiments** take advantage of the radioactive decay of daughter nuclei needing a shorter measuring time. They concentrate on the decays of  $^{232}\text{Th} \rightarrow ^{232}\text{U}$  and of  $^{238}\text{U} \rightarrow ^{238}\text{Pu}$  with characteristic  $Q_{\beta\beta}$  value of 0.85 MeV and 1.15 MeV, respectively.

Generally, the geochemical and the radiochemical experiments, as a consequence of their principle, provide less information about  $\beta\beta$  decay, including the limited sensitivity in comparison with the other types of experiments mentioned.

**Semiconductor experiments** use active type of sources where both the source and the detector are made of  $^{76}\text{Ge}$ . They provide an excellent energy resolution ( $\approx 5$  keV at 2 MeV) but they cannot provide tracking of particles. Their improvement is based on using the enriched High-Purity Germanium (HPGe) detectors, on the background reduction and on the improvement of the analysis systems to distinguish between the single-site ( $\beta\beta$  decay) and the multi-site (multiple Compton scattering) events.

**Scintillator experiments** use scintillators containing  $\beta\beta$  decay isotopes: for example  $^{48}\text{Ca}$  in the form of  $\text{CaF}_2$ , or  $^{116}\text{Cd}$  in the form of  $\text{CdWO}_4$ . They can be produced in larger amount in comparison with  $^{76}\text{Ge}$  but the energy resolution is poor (10 % at 661 keV).

**Cryogenic experiments** use bolometers working at a very low temperature of several mK. Studies using  $^{130}\text{Te}$  in the form of  $\text{TeO}_2$  crystals have been performed.

**Wire chambers or TPC experiments** use passive type of sources where the emitters are either in the form of the filling gas ( $^{136}\text{Xe}$ ) of the detection chamber or in the form of thin foils ( $^{82}\text{Se}$ ,  $^{96}\text{Zr}$ ,  $^{100}\text{Mo}$ ,  $^{116}\text{Cd}$ ,  $^{150}\text{Nd}$ ) in different geometrical configuration (cylindrical, planar). They allow energy measurements and tracking of electrons. The disadvantages are the energy resolution and the limited amount of source.

### 1.3 Isotope $^{116}\text{Cd}$

Cadmium is an element with 48 protons. Up to now, 36 cadmium isotopes are known which have the mass number from 96 to 131 (eight of them can be in metastable state). Cadmium was discovered by Friedrich Strohmeyer (Germany) in 1817. The origin of its name comes from the Latin word *cadmia* meaning calamine (zinc carbonate,  $\text{ZnCO}_3$ ), or from the Greek word *kadmeia* with the same meaning, reflecting the fact that cadmium is extracted principally as a byproduct from processing the sulfide ores of zinc (or also of lead and copper). Thanks to its properties, cadmium is widely used on one hand for production of some of the lowest melting alloys, solder and bearing alloys, on the other hand for electroplating, phosphors in television tubes or for the various painting pigments, even for stabilizers in PVC. Cadmium, thanks to its large cross section for reactions with low-energy neutrons, also plays a special role in reactor and neutron physics and in neutron dosimetry [13, 14].

The first observation of  $^{116}\text{Cd}$  was made by Aston in 1935 [15] and a more detailed mass-spectrographic study was done by Nier in 1936 [16]. Later, isotope  $^{116}\text{Cd}$  was studied from many points of view. Its main nuclear characteristics are listed in Table 1.2.

It is obvious from Table 1.1 that one of suitable elements for  $\beta\beta$  decay measurement is  $^{116}\text{Cd}$  which disintegrates into  $^{116}\text{Sn}$  (Figure 1.3).

The first  $\beta\beta$  decay experiment with  $^{116}\text{Cd}$  was realized by Winter in 1955 [18]. Winter used a random Wilson cloud-chamber and, with the respect of the used method, he obtained fantastic half-life limit.

Quantity	Value
Relative atomic mass ( $A_{rel}$ )	115.904755(3)
Mass excess ( $\Delta$ )	-88719(3) keV
Binding energy ( $E_{bind}$ )	8512.41(3) keV
Neutron separation energy ( $S_n$ )	8700.2(20) keV
Proton separation energy ( $S_p$ )	11021(35) keV
Double beta decay energy ( $Q_{\beta\beta}$ )	2809(4) keV
Ground-state spin and parity ( $J^\pi$ )	$0^+$
Natural abundance ( $\eta$ )	7.49(12)%
Production mode	Naturally occurring Fission product

Table 1.2: The basic nuclear characteristics of  $^{116}\text{Cd}$ . Ref. [17].

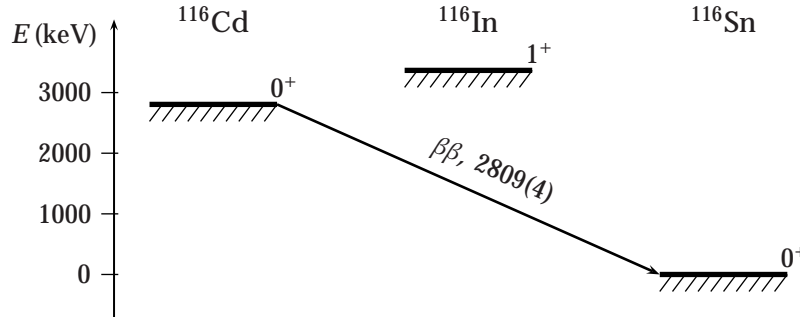


Figure 1.3: The  $\beta\beta$  decay scheme of  $^{116}\text{Cd}$ .

The next experiment was not realized until 1987 when Mitchell and Fischer improved Winter's value only little [19]. The situation changed in the nineties of 20th century when, thanks to the progress in detection technologies, three experiments (NEMO, ELEGANT and Solotvina) measured this value precisely and gave contemporary values. The historical overview of results is summarized in Table 1.3.

Experiment	$T_{1/2}^{2\nu\beta\beta}$ (yr)	Year	Ref.
Winter	$\geq 1 \times 10^{17}$	1955	[18]
Mitchell and Fischer	$> 5.3 \times 10^{17}$	1987	[19]
ELEGANT	$2.6^{+0.9}_{-0.5} \times 10^{19}$	1995	[20]
NEMO2	$[3.75 \pm 0.35(stat.) \pm 0.21(syst.)] \times 10^{19}$	1996	[21]
SOLOTVINA	$2.9^{+0.4}_{-0.3} \times 10^{19}$	2003	[22]
NEMO3	$[2.7 \pm 0.1(stat.) \pm 0.3(syst.)] \times 10^{19}$	2004	[23]

Table 1.3: Experimentally determined  $\beta\beta$  decay half-lives of  $^{116}\text{Cd}$ .

## Chapter 2

# NEMO experiment

The NEMO (Neutrino Ettore Majorana Observatory) experiment was designed to study especially the  $0\nu\beta\beta$  decay of  $^{100}\text{Mo}$  and  $^{82}\text{Se}$ , but it is also used for measurement of different channels of  $2\nu\beta\beta$  decay (ground state - ground state and ground state - excited state transitions) of several nuclei. The NEMO experiment is located at the Fréjus Underground Laboratory (Modane, France), 4,800 m.w.e. (m.w.e. = meter water equivalent).

Up to now, more than 40 physicists from 7 countries (France, Russia, USA, Czech Republic, UK, Japan, Finland) participate to the NEMO Collaboration.

### 2.1 Research and development prototypes

#### 2.1.1 NEMO1

NEMO1 (1991-1992) was the first technological prototype of this experiment. It had a very simple structure consisting of 64 drift cells working in Geiger mode (Geiger cells) mounted inside a copper box ordered in 8 parallel planes of 8 cells for the 3D event reconstruction (Figure 2.1).

Its aim was to measure and to understand the background in Fréjus laboratory and to prove the feasibility of such project. NEMO1 took data during 18 months in various running conditions. It found out that the background in  $E \lesssim 2$  MeV originates from the natural radioactivity  $\gamma$ -flux; in the region of energies  $3 \text{ MeV} < E < 8 \text{ MeV}$ , the main contribution came from neutrons; and for  $E > 8$  MeV the remaining muon flux was identified [24, 25].

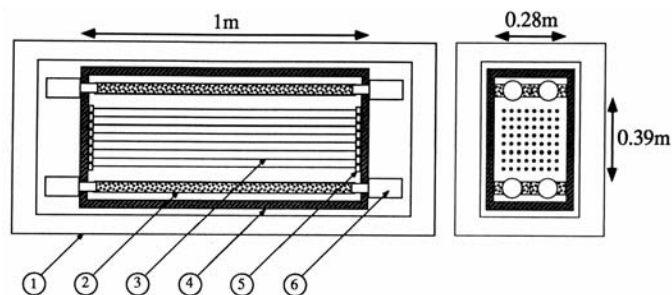


Figure 2.1: The NEMO1 prototype: (1) Shielding, (2) Plastic scintillators, (3) Wires of Geiger cells, (4) Copper wall (1 cm thick), (5) Cathode ring, (6) Phototube. Ref. [24].

#### 2.1.2 NEMO2

NEMO2 (1993-1996) consisted of  $1 \text{ m}^3$  tracking volume filled with helium gas and 4 % admixture of ethylalcohol at the atmospheric pressure. The tracking part was made of octagonal Geiger cells (32 mm

in diameter, 1 m in length), each with a central nickel wire (100  $\mu\text{m}$  in diameter) surrounded by 8 ground wires. On both cell ends, there was a copper ring (29 mm in diameter) used as a pick up electrode. Thanks to the filling gas properties ensuring a good transparency of the wire chamber, electrons with energy down to 100 keV could be detected.

The detector (Figure 2.2) consisted of vertical planes, where the central one contained a source foil ( $1 \times 1 \text{ m}^2$ ). On each side of the source foil, there were 10 planes of 32 Geiger cells each, providing a 3D event reconstruction. Both vertical sides were closed with calorimeter walls made of plastic scintillators. In addition, tracking volume and scintillators were covered with lead and iron shields [25, 26].

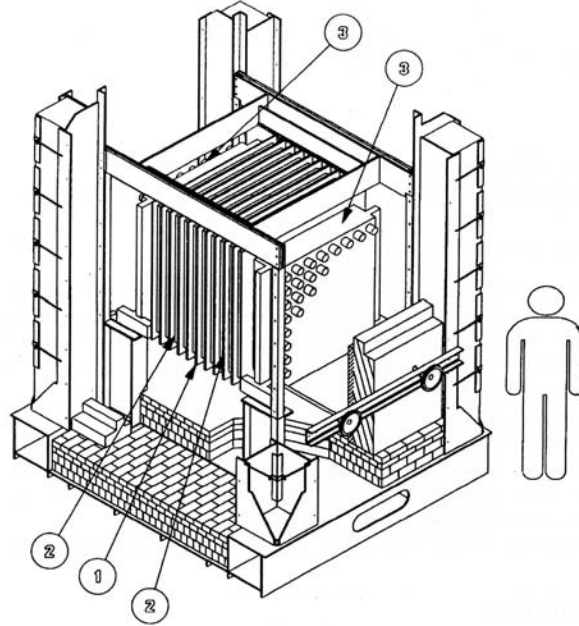


Figure 2.2: The NEMO2 prototype: (1) Central frame with metallic foil, (2) Tracking device of 10 frames with  $2 \times 32$  Geiger cells each, (3) Scintillator walls of  $8 \times 8$  counters. The shielding is not shown. Ref. [26].

NEMO2 took measurement in  $2e$ ,  $e\gamma$ ,  $e\gamma\alpha$  channels. It observed a clear  $2\nu\beta\beta$  signal emanating from pure enriched  $^{100}\text{Mo}$ -foils. The search for one-electron events allowed to put some limits for the  $\beta$  emitter nuclide contamination. Another studies were realized with  $^{82}\text{Se}$ ,  $^{116}\text{Cd}$ , and  $^{96}\text{Zr}$  (Table 2.1); also Cu and natural Mo-foils were used for background measurement.

The radon presence inside of the NEMO2 detector was proved [27]. It implied an additional isolation of the further detectors.

Isotope	$T_{1/2}^{2\nu\beta\beta}$ (yr)	$T_{1/2}^{0\nu\beta\beta}$ (yr)	Ref.
$^{82}\text{Se}$	$8.30 \pm 1.00 \pm 0.70 \times 10^{19}$	$> 9.5 \times 10^{21}$	[28]
$^{96}\text{Zr}$	$2.10^{+0.8}_{-0.4} \pm 0.20 \times 10^{19}$	$> 1.0 \times 10^{21}$	[29]
$^{100}\text{Mo}$	$9.50 \pm 0.40 \pm 0.90 \times 10^{18}$	$> 6.4 \times 10^{21}$	[30]
$^{116}\text{Cd}$	$3.75 \pm 0.35 \pm 0.21 \times 10^{19}$	$> 5.0 \times 10^{21}$	[31]

Table 2.1: The NEMO2 results.

## 2.2 NEMO3 experiment

The NEMO3 detector was constructed on the basis of experience with two technological prototypes NEMO1 and NEMO2. Its design combines tracking device and calorimeter. So, it allows measurement

of energy and time of electrons and photons as well as the 3D tracking of electrons, positrons, and  $\alpha$ -particles.

NEMO3 is aimed to measure the  $0\nu\beta\beta$  decay on the level of  $T_{1/2} \simeq 10^{25}$  yr which corresponds to the effective neutrino mass of the order of (0.1 - 0.3) eV.

### 2.2.1 General description

The NEMO3 experiment is installed in the Fréjus Underground Laboratory (also known as Laboratoire Souterrain de Modane, LSM) in France. The detector (Figure 2.3) has a cylindrical shape (4 m in diameter, 3 m in height) and is divided into 20 equal sectors. The tracking volume ( $27 \text{ m}^3$ ) is filled with helium with admixture of 4 % ethylalcohol and 1 % argon. The whole system uses 6,180 Geiger cells (2.7 m in length) parallel to the vertical axis of the detector. The inner and outer walls of the detector interior are covered by the calorimeter made of 1,940 plastic scintillators which are coupled to low-radioactive PMTs and which serve for time and energy measurement. The source foils form a thin middle layer in the sectors and divide the wire chamber into two concentric parts.

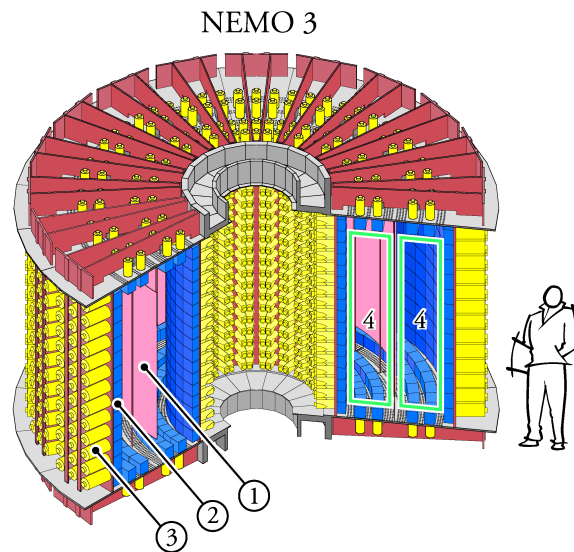


Figure 2.3: Schematic view of the NEMO3 detector core without external shielding: (1) source foils, (2) 1,940 plastic scintillators coupled to (3) low-activity photomultiplier tubes, (4) tracking volume with 6,180 drift cells operating in Geiger mode. Ref. [23].

A vertical magnetic field of 25 Gauss generated by the solenoid surrounding the detector is used to identify the particle charge and, thus, to eliminate the background contribution of pair creation and incoming electrons crossing the detector. The shielding is provided by low-radioactive iron, wood, polyethylene and borated water in order to suppress efficiently external background. Monte-Carlo (MC) simulations as well as data analysis show that the main remaining source of background is radon which penetrated from the air of the LSM lab inside the detector. Thanks to the great contribution of radon on the total background, the anti-radon device cleaning air is planned to be installed during the autumn 2004. It will reduce the background from radon by a factor of about 50.

The NEMO3 detector allows the registration of electrons, positrons, photons and  $\alpha$ -particles. So, it is possible to define various channels for different signal and background studies [26, 32].

### 2.2.2 Tracking wire chamber

The tracking wire chamber of NEMO3 provides 3D tracking of charged particles. It is made up of 6,180 Geiger cells (270 cm long, 3 cm in diameter) which are stretched in layers between top and bottom

endcaps of sectors. Each cell is composed of one anodic (operating voltage of 1,800 V) and eight or nine (depending on their position in the detector) ground cathodic stainless steel wires with a diameter of 50  $\mu\text{m}$ . Two or three cathodic wires are shared with each neighbouring cell. The "4-2-3" layer configuration in each half of a sector, meaning four cell layers near the source foil followed by a gap, then two cell layers and another gap followed by three cell layers near the scintillator wall, is used (Figure 2.4). The gaps between the groups of cell layers are due to the position of the plastic scintillators on the endcaps. The four layers near the source foil are sufficient to provide a precise vertex position. Two layers in the middle and three layers close to the plastic scintillator walls provide good trajectory curvature measurements.

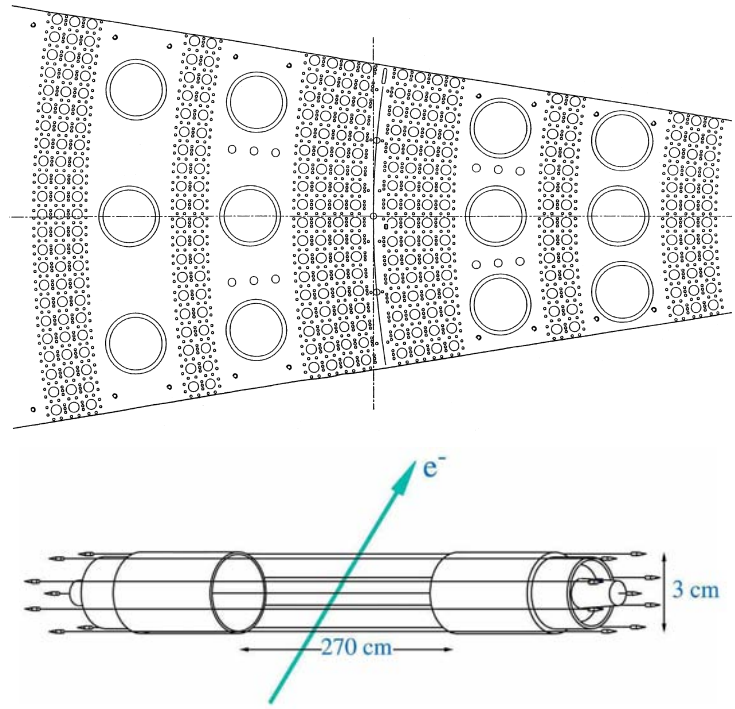


Figure 2.4: Up: The Geiger cell layout in a sector (top view). Down: A scheme of an elementary Geiger cell. Ref. [32].

The geometry allows electrons to drift towards the anode with speed of  $(1.0 - 2.3) \text{ cm}/\mu\text{s}$  depending on the distance from the anode; corresponding anodic pulse has a fast rise within 10 ns. In Geiger regime, an avalanche originating near the anode develops into the Geiger plasma which propagates along the wire at a speed of about  $(6 - 7) \text{ cm}/\mu\text{s}$ . The arrival of the plasma at the ends of the wire is detected with the cathode rings (3 cm in length, 2.3 cm in diameter). The anode wire runs through the center of this ring while the ground wires are supported just outside the ring. The propagation times, which are measured this way, are used then for the determination of the longitudinal position of the particle as it passes through the cell [32].

### 2.2.3 Calorimeter

The calorimeter of NEMO3 is aimed for energy measurement of electrons (or positrons) in the range of  $(0.15 - 12.00) \text{ MeV}$ , and of photons in the range of  $(0.08 - 12.00) \text{ MeV}$ . It also provides time measurement which is important for rejection of external background events using appropriate time-of-flight (TOF) criteria.

The NEMO3 calorimeter is composed of 1,940 blocks of plastic scintillators coupled with a light guide to very low radioactivity Hamamatsu photomultiplier tubes (PMTs). PMTs are of two sizes: 3"

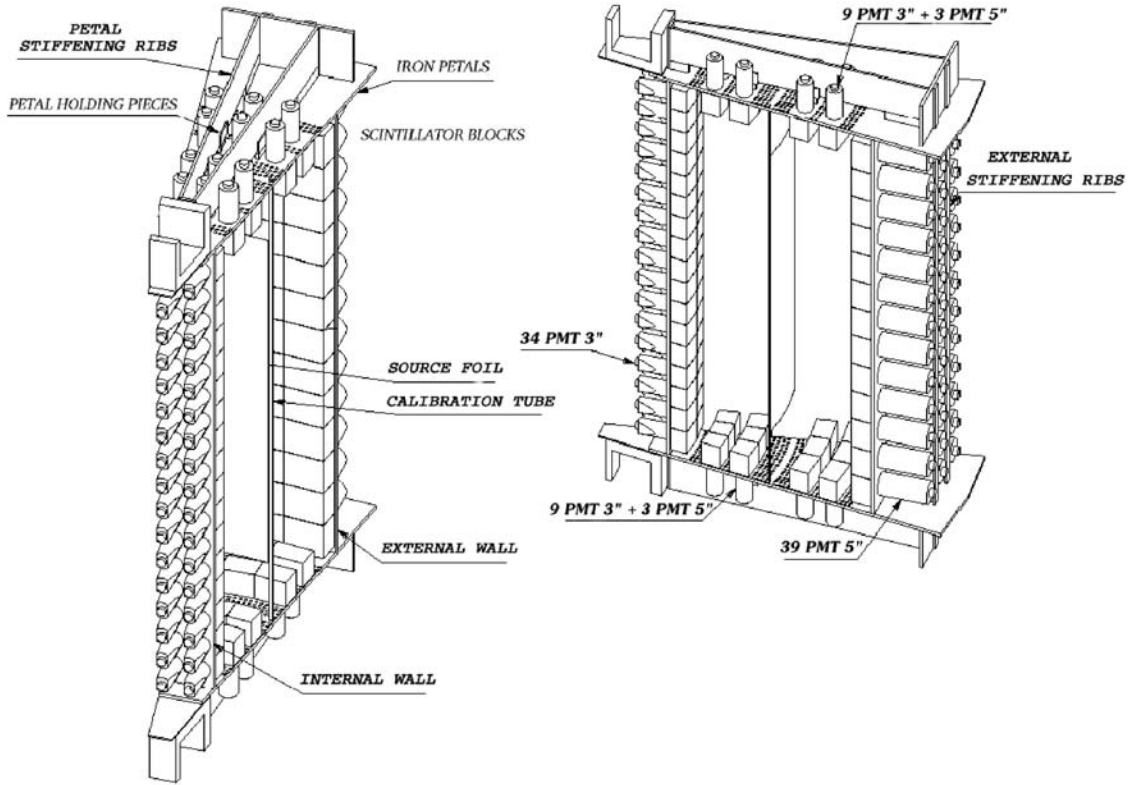


Figure 2.5: The scheme of one NEMO3 sector. Ref. [32].

and 5". Each sector is equipped with 97 scintillator blocks as follows: 34 scintillators on the internal wall (two columns of 17 counters), 39 scintillators on the external wall (three columns of 13 counters), 12 scintillators on the upper endcap and another 12 on the bottom endcap (Figure 2.5).

The NEMO3 scintillators are made of polystyrene (PST, 98.49 %) with addition of p-terphenyl (PTP, 1.5 %) and the wavelength shifter 1, 4-di-(5-phenyl-2-oxazolyl)benzene (POPOP, 0.01 %) [32]. The mechanical protection of scintillators is ensured by wrapping them in aluminized mylar foil (6  $\mu\text{m}$  thick mylar foil, 0.3 nm thick aluminium layer). Furthermore, the lateral faces of each scintillator block are covered with 5 layers of a teflon band (each 70  $\mu\text{m}$  thick) in order to reflect light back inside the scintillators and thus increases the light collection efficiency.

Very low radioactivity Hamamatsu PMTs have activities in  $^{214}\text{Bi}$ ,  $^{208}\text{Tl}$ , and  $^{40}\text{K}$  three orders of magnitude below standard PMTs; the main contribution comes from the PMT glass [32]. Measured activities in  $^{214}\text{Bi}$  and  $^{208}\text{Tl}$  of the NEMO3 PMTs are summarized in Table 2.2.

Total activity in Bq	$^{40}\text{K}$	$^{214}\text{Bi}$	$^{208}\text{Tl}$
3" PMTs R6091 - 1040 pieces (230 g/PMT)	354	86	5.2
5" PMTs R6594 - 900 pieces (385 g/PMT)	477	216	12.6
Sum	831	302	17.8

Table 2.2: Total radioactivity of NEMO3 Hamamatsu Photomultipliers. Ref. [32].

The PMTs are closed in black plastic boxes to protect them from the ambient light. All the PMTs are also screened from the magnetic field generated by the coil (section 2.2.5) with cylindrical  $\mu$ -metal shields.

The energy resolution  $\sigma(E)/E$  of the NEMO3 calorimeter is (6 – 7) % at 1 MeV. The time resolution at 1 MeV is about 250 ps. The time measurement is important especially for the NEMO3 trigger and data analysis of events. The TOF information is indispensable for the efficient rejection of external

background events during the data analysis [32, 33].

Daily survey of the calorimeter is provided by a laser-based system which is incorporated into the NEMO3 calorimeter. This daily survey is important because certain parameters like the PMT gain can vary over time. In this system, a small bulbous scintillator converts the laser pulse into a properly shaped and wavelength-shifted (420 nm) signal which simulates one-electron events in the scintillator. This light is then delivered by optical fibres to each of the photomultipliers in the calorimeter and to six reference PMTs. An accuracy of 1 % for the energy gain is assured via a comparison of the laser light stability with the six reference PMTs that are continuously exposed to  $^{207}\text{Bi}$  sources.

Each sector has a calibration tube which is placed in the central source foil vertical plane (Figure 2.5). This flattened, rectangular profile, copper tube has three kapton windows on each side: at the bottom, central, and top levels. A plastic carrier with three calibration sources corresponding to the tube window positions can be inserted inside the tube from the upper part of each sector. This system was also used for the PMT time and gain alignments, for various tests of the trigger and data acquisition systems, and for measurements of the track reconstruction performance of the wire chamber. Sources of  $^{207}\text{Bi}$ ,  $^{90}\text{Sr}$ , and  $^{106}\text{Ru}$  are used for the energy calibration and for the tests of the tracking wire chamber while sources of  $^{60}\text{Co}$ , which emit two photons of 1333 keV and 1173 keV in coincidence, are used for the time alignment [33, 34].

## 2.2.4 NEMO3 sources

The NEMO3 experiment is intended on study of  $\beta\beta$  decay of several isotopes:  $^{100}\text{Mo}$ ,  $^{82}\text{Se}$ ,  $^{116}\text{Cd}$ ,  $^{130}\text{Te}$ ,  $^{150}\text{Nd}$ ,  $^{96}\text{Zr}$ , and  $^{48}\text{Ca}$ . Source materials were selected with the respect of several criteria. One of them is the high value of transition energy  $Q_{\beta\beta}$  (Table 1.1) in order to avoid background events in the  $0\nu\beta\beta$  decay region. Main problems are connected with  $^{208}\text{Tl}$  giving 2.615 MeV  $\gamma$ -rays, thus, all investigated isotopes have higher  $Q_{\beta\beta}$  value. Other criteria are the values of nuclear matrix elements for  $2\nu\beta\beta$  and  $0\nu\beta\beta$  processes and the natural abundance ( $\geq 2\%$ ) of studied isotopes in order to produce highly enriched materials.

The main goal of NEMO3 experiment is to measure the  $0\nu\beta\beta$  decay of  $^{100}\text{Mo}$  and  $^{82}\text{Se}$ . These isotopes fill the biggest part of the detector. Such sources have the highest masses and enrichment, and their impurities are on the lowest technologically reachable level. The rest of isotopes, except natural tellurium and copper, are intended for very accurate measurement of  $2\nu\beta\beta$  decay. Copper and natural tellurium serve for determination of external background. A review of all the NEMO3  $\beta\beta$  isotopes is given in Table 2.3.

Source	Type	$M_1$ (g)	$M_2$ (g)	$M_3$ (g)	Enrichment (%)	Sector	Studied process
$^{100}\text{Mo}$	composite	5578.29	4604.72	4434.61	95.14 - 98.95	01, 05, 10 - 16	$0\nu\beta\beta$ , $2\nu\beta\beta$
	metallic	2545.75	2542.03	2478.94	95.14 - 98.90	01 - 05	$0\nu\beta\beta$ , $2\nu\beta\beta$
$^{82}\text{Se}$	composite	1127.07	962.02	932.39	96.82 - 97.02	06 - 08	$0\nu\beta\beta$ , $2\nu\beta\beta$
$^{130}\text{TeO}_2$	composite	756.38	507.78	453.90	89.4	09, 17	$0\nu\beta\beta$ , $2\nu\beta\beta$
$^{116}\text{Cd}$	metallic	491.18	434.42	404.89	93.3	18	$0\nu\beta\beta$ , $2\nu\beta\beta$
$^{150}\text{Nd}_2\text{O}_3$	composite	56.68	40.18	36.55	91.0	05	$0\nu\beta\beta$ , $2\nu\beta\beta$
$^{96}\text{ZrO}_2$	composite	26.51	16.42	9.41	57.3	05	$2\nu\beta\beta$
$^{48}\text{CaF}_2$	composite	18.516	9.572	6.997	73.1	05	$2\nu\beta\beta$
$^{\text{nat}}\text{TeO}_2$	composite	893.62	491.08	165.98	–	08, 19	background
$^{\text{nat}}\text{Cu}$	metallic	620.80	620.80	620.80	–	00	background

Table 2.3: Characteristics of the source foils of the NEMO3 sectors;  $M_1$ ,  $M_2$  and  $M_3$  mean the total masses of material, of the investigated element, and of the relevant  $\beta\beta$  decay isotope in the foils, respectively. Ref. [32].

All the sources have a form of thin foils. Their thickness was chosen with the respect to energy resolution which is fixed by calorimeter design. The mean surface densities are between 30 and 60 mg/cm<sup>2</sup>. Furthermore, foils are either of metallic or composite type. Composite foils are produced as a mixture of source powder and organic glue which is closed between two Mylar sheets forming a sandwich-like structure. All the foils (2,480 mm in length, 65 mm in width) are placed into source frames and introduced into individual sectors (7 foil strips by sector). Figure 2.6 shows arrangement by sectors of the NEMO3 sources.

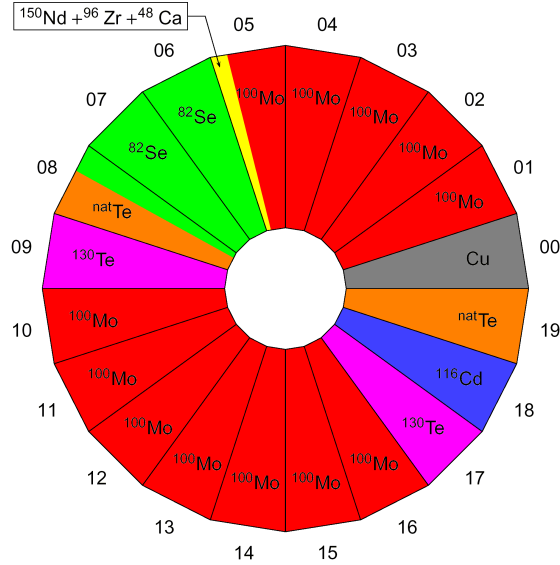


Figure 2.6: The NEMO3 source arrangement. Ref. [32].

### <sup>116</sup>Cd source

The metallic enriched cadmium was obtained by the centrifuged separation method. The enrichment of <sup>116</sup>Cd is (93.2 ± 0.2) %. Part of the sample was measured with the NEMO2 prototype [31]. Another part was purified by a distillation technique [35]. Despite the metallic form of the cadmium source, the strips were glued between Mylar foils to provide mechanical strength in the vertical position. A total mass of (405 ± 1) g of <sup>116</sup>Cd was placed in sector 18 [32]. More detailed information about the <sup>116</sup>Cd source is given in Table 2.3. The radioactivity limits of the sources, which were obtained with HPGe detectors, are listed in Table 2.4.

Source sample activity (mBq/kg)	Measured mass (g)	Exposure (h)	<sup>40</sup> K	<sup>235</sup> U		<sup>238</sup> U		<sup>232</sup> Th	
				<sup>207</sup> Tl, <sup>211</sup> Pb	<sup>234</sup> Th	<sup>214</sup> Bi, <sup>214</sup> Pb	<sup>228</sup> Ac	<sup>208</sup> Tl	
<sup>116</sup> Cd + Mylar	257	778	< 13.000	< 0.500	< 12.000	< 1.500	< 2.000	< 0.500	
	299	368	< 20.000	< 1.000	< 56.000	< 1.700	< 4.000	< 0.830	
Total activity			< 16.764	< 0.769	< 35.662	< 1.608	< 3.076	< 0.677	

Table 2.4: The radioactivity limits for impurities in the NEMO3 Cd source (in mBq/kg). Ref. [32].

### 2.2.5 Reduction of external backgrounds

**Iron shield** As the first external background barrier of the NEMO3 detector, an external low radioactivity iron shield is used. It is composed of 20 cm thick low radioactivity iron plates which are attached to the external mechanical frame (Figure 2.7). Its role is to reduce  $\gamma$ -rays and thermal neutrons coming from the LSM laboratory. Previous MC studies with NEMO2 [36, 37] showed the iron shield to be

very efficient to suppress  $\gamma$ -rays. Furthermore, it completely absorbs thermal neutrons. In the case of epithermal and fast neutrons an effect is lower, thus, an extra neutron shielding is used.

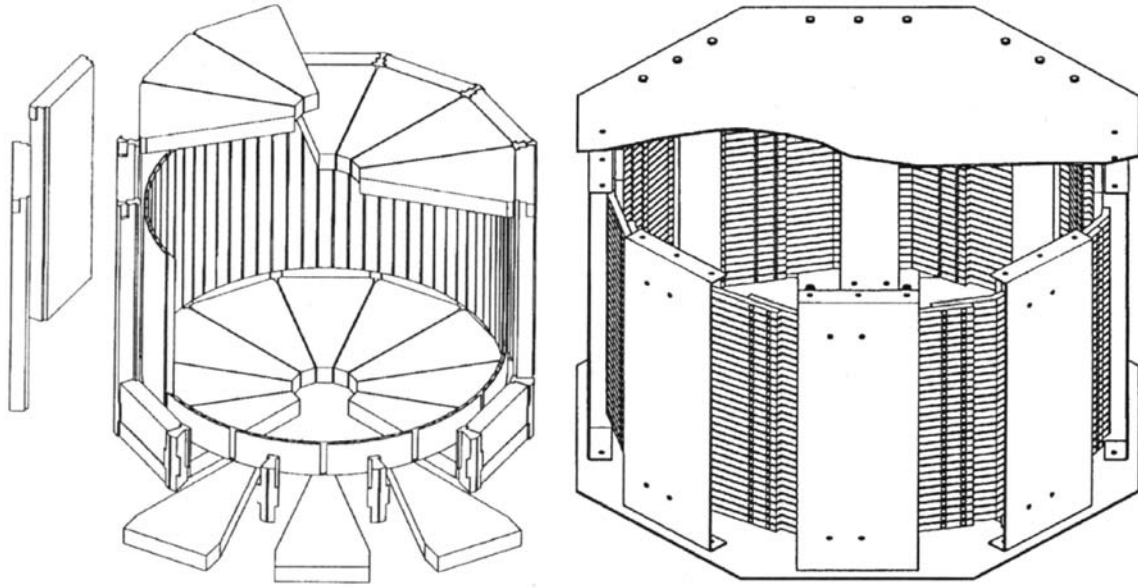


Figure 2.7: The shielding of NEMO3 detector. Left: The scheme of the iron shield. Right: The layout of magnetic coil. Ref. [33].

**Neutron shielding** Fast and epithermal neutrons from the LSM laboratory can pass through the iron shield. After their moderation in plastic scintillators, they can be captured by copper nuclei of the NEMO3 frame and high energy deexcitation photons can be then generated. To thermalize these neutrons before reaching the iron shield which will stop them completely, an additional outer shielding was built. It is composed of 10 water tanks made from stainless steel and fixed to the external mechanical frame of the detector. These tanks have an internal capacity of 2.5 m<sup>3</sup> and provide a 34 cm layer of borated water. To cover the top and the bottom of the detector the wooden blocks of 28 cm thickness are currently used.

**Magnetic field** A high energy photon interacting with the NEMO3 source foils can produce an electron-positron pairs inside the detector. They will have the same signature as the two-electron events from double beta decay in the foils. Consequently, the pair production is a dangerous kind of background for neutrinoless double beta decay. To distinguish between the  $e^+e^-$  pairs and the  $2e^-$  events, the curvatures of tracks in magnetic field is used, so, a vertical magnetic field of 25 Gauss is applied in the NEMO3 experiment. This field is generated by a coil (Figure 2.7) surrounding the detector and placed between the external wall of the detector and the iron shield. The coil is made of copper rods and is divided into ten segments (one segment covers two sectors) which are interconnected to form compact solenoid spirals [33].

## 2.2.6 Trigger

The NEMO3 trigger treats data from the tracking wire chamber and calorimeter for each event candidate independently. So, it does not need the complete information from the wire chamber and calorimeter for each event. Instead of information from all the fired Geiger cells, it deals with the Geiger cell rows in each sector, and it is limited to the horizontal x-y plane of the detector completely ignoring the vertical direction (the z-coordinate of a Geiger cell hit). The trigger uses information about the scintillator walls

involved in an event and the total multiplicity of involved scintillator/PMT counters instead of the information from each fired scintillator.

The trigger selects good physical events through processing first a rough track recognition, based mainly on the information from Geiger cell rows. Then the selection is refined by searching for a geometric correlation between these Geiger cell rows and the scintillator walls involved in the event candidate [40].

The trigger system is designed with three levels T1, T2, and T3. The first one (T1) is based only on the PMT multiplicity. The second level (T2) consists of the track recognition in the tracking wire chamber and is performed on a half-sector basis. Finally, the third level (T3) consists of the check for a possible coincidence between pre-tracks from the T2 level and fired scintillator walls [33].

### 2.2.7 Data acquisition system and detector monitoring

The data acquisition system uses two boards, one for the calorimeter data processing and the other for the tracking detector data processing. If the trigger criteria are satisfied, then both these processors record into their registers the calorimeter and tracking detector data. After that, the trigger system synchronizes both parts and gets ready for the next event acquisition. Afterwards, the data from both processors are sent to the event-builder board and saved in an n-tuple file. While both processors are independent one on another, the acquisition system also allows running the data acquisition only with the calorimeter without the tracking detector and vice versa. The data acquisition rate can vary from a few Hz for normal  $\beta\beta$  decay runs (typically  $\sim 7$  Hz) to several kHz for calibration runs with radioactive sources introduced inside the detector.

The detector monitoring is provided by two PCs installed in the LSM laboratory. Their role is to read different data and parameters and allow the operators to check via the graphic interface the status and values of electric boxes, crates, high voltage boards for both the calorimeter and the wire chamber, gas pressure and temperature from the detector gas supplying system, voltage and current supplying the magnetic coil and so on. Another very important feature of this survey system is that the graphic interface allows turning the calorimeter and tracking Geiger counters either on or off and also to change their high voltage values. Both the data acquisition and detector monitoring can be performed from local (inside the LSM laboratory) or remote computers [33].

## 2.3 NEMO3 background

### 2.3.1 Background of the experiment

The  $\beta\beta$  decay processes are characterized by very long half-lives. For their efficient measurement, there is a great effort to reduce background as much as possible. So, background is the most significant concern in  $\beta\beta$  measurements in the whole energy range - from low energies (easy discriminated by selection criteria), but also in the  $Q_{\beta\beta}$  value region. A large part of background sources comes from natural radioactive chains and from other long-life isotopes occurring inside materials of the source foils and the detector. Another contribution comes from the air contamination by radon and thoron.

### 2.3.2 Internal background

The internal background is connected with source materials where, due to different effects (Figure 2.8), the two-electron events simulating  $\beta\beta$  decay occur. The main sources are naturally occurring impurities which amount depends on a locality of origin of the primary ores and on the methods of their treatment and purification. Because of high  $Q_{\beta\beta}$  values, the most dangerous isotopes are  $^{214}\text{Bi}$ , giving  $\beta$ -particles with energy up to 3.27 MeV,  $\gamma$ -rays with energies up to 2.62 MeV and  $\alpha$ -particles with 5.62 MeV, and  $^{208}\text{Tl}$ , giving 5.00 MeV  $\beta$ -particles, and photons with energy up to 1.76 MeV. Mainly the two-electron events are created via  $\beta$  decay accompanied by an internal conversion (Figure 2.8a),  $\beta$  decay

accompanied by Compton effect (Figure 2.8b) or via  $\beta$  decay followed by Möller scattering (Figure 2.8c) [33].

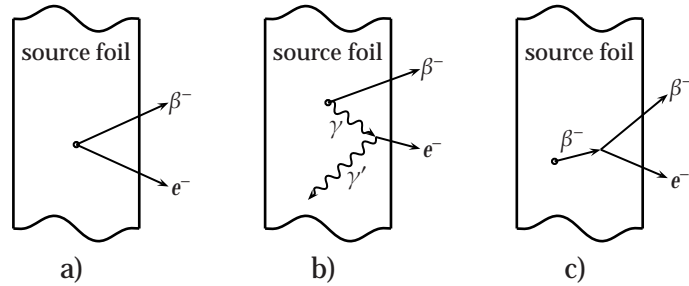


Figure 2.8: Internal background processes generating two-electron events.

### 2.3.3 External background

The external background in NEMO3 experiment is defined as the events produced by  $\gamma$ -rays coming from outside of the source foils which interact with the foils. These interactions can lead to two-electron events by pair creation (Figure 2.9a), double Compton scattering (Figure 2.9b), Compton effect followed by Möller scattering (Figure 2.9c), photoelectric effect followed by Möller scattering (Figure 2.9d), or by Compton scattering followed by the photoelectric effect (Figure 2.9e) [32, 33].

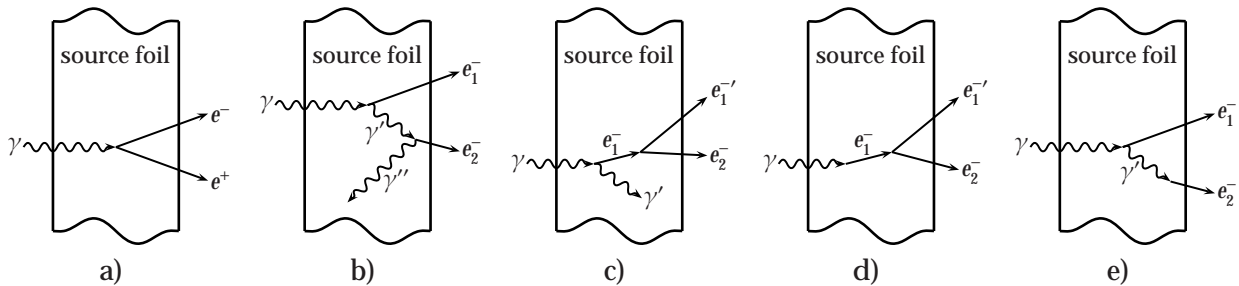


Figure 2.9: External background processes generating two-electron events.

Due to the natural activity, there is a need to use low-radioactivity materials for detector construction. The most important sources of the natural background are the isotopes with very long half-life like potassium, uranium and thorium together with their daughters. The most problematic isotopes are  $^{214}\text{Bi}$  and  $^{208}\text{Tl}$ , which cause the main part of two-electron events in the (2.8 – 3.2) MeV energy window which is used in NEMO3 for  $0\nu\beta\beta$  decay search [32, 33].

### 2.3.4 Radon and thoron

Radon and thoron are noble radioactive gases originating from uranium and thorium decay chains, respectively (Figure 2.10). They are produced in laboratory surrounding rocks through which they penetrates into the laboratory air. The vigorous air ventilation system in the laboratory reduces radon levels down to (10 – 20) Bq/m<sup>3</sup>. However, it enters inside of the detector by diffusion through leakage places on the detector covering surface. Even if it decays before ingress into the detector, a danger still exists because of its daughter isotopes. They can be transported by dust and deposited on the detector. Radon can also enter the detector through the gas supply system. This can happen if bottles of helium gas already contain some quantity of radon, or if the pipes and joints of the gas system are not airtight enough. Radon has three isotopes corresponding to the three decay chains: radon  $^{222}\text{Rn}$ , thoron  $^{220}\text{Rn}$ , and actinon  $^{219}\text{Rn}$ . Generally, actinon gas is not dangerous for the experiment because its daughters do not have enough available energy to generate background events that could

be confused with  $\beta\beta$  decay, in comparison with radon and thoron which daughters are  $^{214}\text{Bi}$  and  $^{208}\text{Tl}$ , respectively [33].

	$^{238}\text{U}$					$^{232}\text{Th}$					
U	U-238 4.47 10 <sup>9</sup> yr		U-234 2.45 10 <sup>5</sup> yr								
Pa	↓	Pa-234 1.17 m	↓		β ↗						
Th	Th-234 24.1 d		Th-230 75400 yr		α ↓		Th-232 14 10 <sup>9</sup> yr		Th-228 1.913 yr		
Ac			↓				Ac-228 6.15 h		↓		
Ra			Ra-226 1600 yr				Ra-228 5.75 yr		Ra-224 3.66 d		
Fr			↓						↓		
Rn			Rn-222 3.824 d						Rn-220 55.6 s		
At			↓						↓		
Po		Po-218 3.10 m		Po-214 164 μs		Po-210 138.4 d			Po-216 145 ms		Po-212 300 ns
Bi		↓	Bi-214 19.9 m		Bi-210 5 d				↓	Bi-212 60.5 m	↓
Pb		Pb-214 26.8 m	0.02% ↓	Pb-210 22.3 yr		Pb-206 stable			Pb-212 10.6 h	36% ↓	Pb-208 stable
Tl			Tl-210 1.3 m		Tl-206 4.19 m					Tl-208 3.1 m	

Figure 2.10: The  $^{238}\text{U}$  and  $^{232}\text{Th}$  decay chains. The decays of radon  $^{222}\text{Rn}$  to  $^{214}\text{Bi}$  and of thoron  $^{220}\text{Rn}$  to  $^{208}\text{Tl}$  are bounded by shadowed cells. Ref. [33].

### 2.3.5 Neutrons

Neutrons are products of spontaneous fission or the  $(\alpha, n)$  reaction of radioactive impurities in construction materials of the detector or in the rocks surrounding the laboratory. Generally, they are always present inside underground laboratories and their contribution to background is important for  $0\nu\beta\beta$  decay. If neutrons are thermalized and captured in the detector copper frame via  $(n, \alpha)$  or  $(n, p)$  reactions, it presents low danger for  $0\nu\beta\beta$ -channel in comparison with the  $(n, \gamma)$  reaction in iron or copper when photons with energy up to 8 MeV are produced. Fortunately, their influence can be well suppressed by neutron shielding (section 2.2.5) [33, 37].

### 2.3.6 Photons from laboratory surrounding and cosmic rays

Depending on the energy range, the  $\gamma$ -rays come from the natural radioactivity in the surrounding rocks, from radiative neutron capture, and from muon bremsstrahlung. The  $\gamma$ -ray flux in the LSM laboratory has been studied with a low-background NaI detector [36]. In the region below 4 MeV, the obtained energy spectrum is dominated by  $\gamma$ -rays from natural radioactivity in the surrounding material and rocks and is characterized by a maximum at 2.6 MeV ( $^{208}\text{Tl}$ ). In the (4 – 6) MeV energy region the measured spectrum is dominated by the residual internal activities from the uranium and thorium decay chains present inside the NaI crystal, and no contribution from the external natural radioactivity can be found above 6 MeV. Between 6 and 10 MeV, the  $\gamma$ -ray flux is strongly correlated to the neutron flux and is due to the radiative capture of neutrons in Cu, Fe, Pb etc. Above 10 MeV, the

counting rate drops drastically and is due to the bremsstrahlung from the remaining but very small muon flux inside the laboratory. The muon flux in the LSM laboratory is about  $4.9 \times 10^{-5} \text{ m}^{-2} \text{ s}^{-1}$  ( $4.2 \text{ m}^{-2} \text{ day}^{-1}$ ) [38] and is  $2 \times 10^6$ -times lower [39] than the flux at the sea level [33].

### 2.3.7 Detector radiopurity

In  $\beta\beta$  decay experiments the activity of all the materials and components used for detector construction has to be as low as possible. Thus activity measurements, based on  $\gamma$ -spectroscopy, are essential for these experiments especially during the research and development phase when the best construction materials should be selected. As regards the NEMO3 experiment, activity measurements of a great number of samples (construction materials, electronics components, cables, glues and so on) have been carried out with low background HPGe detectors over a few years in the LSM laboratory. The abundance of radioactive isotopes in a sample is determined from the strength of  $\gamma$ -lines in the spectrum obtained with a  $\gamma$ -ray spectrometer. For the purified source foils, only the upper limits of activities at 90 % CL are determined; an overview for the NEMO3 source foils is given in Table 2.5, and the activities for the main NEMO3 detector components are listed in Table 2.6.

Source sample activity (mBq/kg)	Measured mass (g)	Exposure (h)	$^{40}\text{K}$	$^{235}\text{U}$		$^{238}\text{U}$		$^{232}\text{Th}$	
				$^{207}\text{Tl}, ^{211}\text{Pb}$	$^{234}\text{Th}$	$^{214}\text{Bi}, ^{214}\text{Pb}$	$^{228}\text{Ac}$	$^{208}\text{Tl}$	
$^{100}\text{Mo}$ (M)	733.00	840	< 5.0	$1.5 \pm 0.3$	< 15	< 0.39	< 0.5	< 0.11	
$^{100}\text{Mo}$ (C)	735.00	648	< 6.0	< 0.3	< 15	< 0.34	< 0.3	< 0.10	
$^{82}\text{Se}$ (C)	800.00	628	$55.0 \pm 5.0$	$20.0 \pm 0.7$	< 18	$1.2 \pm 0.50$	< 1.0	$0.40 \pm 0.10$	
	292.00	500	$200.0 \pm 20.0$	$8.5 \pm 0.9$	< 25	< 4.20	< 4.0	< 0.70	
$^{130}\text{TeO}_2$ (C)	633.00	666	< 8.0	< 0.5	< 20	< 0.67	$1.7 \pm 0.7$	< 0.46	
$^{116}\text{Cd}$ (M) + Mylar	257.00	778	< 13.0	< 0.5	< 12	< 1.50	< 2.0	< 0.50	
	299.00	368	< 20.0	< 1.0	< 56	< 1.70	< 4.0	< 0.83	
$^{150}\text{Nd}_2\text{O}_3$ (C)	58.20	458	< 70.0	< 1.0	< 66	< 3.00	$20.0 \pm 7.0$	$10.00 \pm 2.00$	
$^{96}\text{ZrO}_2$ (C)	13.70	624	< 217.0	< 7.0	< 222	< 16.00	< 23.0	< 10.00	
	16.60	456	$583.0 \pm 167.0$	< 10.0	< 211	< 14.00	< 27.0	< 5.50	
$^{48}\text{CaF}_2$ (C)	24.56	1590	< 50.0	< 2.0	< 15	< 4.00	< 6.0	< 2.00	
$^{nat}\text{TeO}_2$ (C)	620.00	700	$8.0 \pm 3.0$	< 0.3	< 17	< 0.17	< 0.9	< 0.09	
Cu (M)	1656.00	853	< 8.0	< 0.2	< 5	< 0.12	< 0.4	< 0.04	

Table 2.5: Radioactivity measurements of the NEMO3 source foils (in mBq/kg). The error bars are statistical uncertainties at the  $1\sigma$  level while the limits are at the  $2\sigma$  level. A systematic uncertainty of about 10 % is associated with the MC computations for the HPGe detector efficiencies. Only the lower limits obtained for  $^{100}\text{Mo}$  are presented, for both metallic and composite strips. In the case of  $^{48}\text{CaF}_2$  the results are for the powder. Ref. [32].

Components of NEMO3	Weight (kg)	Total radioactivity (Bq)			
		$^{40}\text{K}$	$^{214}\text{Bi}$	$^{208}\text{Tl}$	$^{60}\text{Co}$
Photomultiplier Tubes	600	831	302	17.8	–
Scintillator blocks	6400	< 102	< 1.2	< 0.6	< 3
Copper	25000	< 125	< 25.0	< 10	< 6
Iron endcaps	10000	< 50	< 6	< 8	$17 \pm 4$
$\mu$ -metal PMT shield	2000	< 40	< 4	< 4	< 4
Tracking detector wires	1.7	$< 8 \times 10^{-3}$	$< 10^{-3}$	$< 6 \times 10^{-4}$	$< 10^{-2}$
Iron shield	180000	< 3000	< 400	< 300	< 600

Table 2.6: Total radioactivity for the main NEMO3 detector components. Ref. [32].

## Chapter 3

# Monte-Carlo simulations

### 3.1 Software tools

All the MC simulations were carried out with the help of program package *nemos* [41], which was developed for the NEMO3 experiment at Institut de Recherches Subatomiques, Strasbourg, and Joint Institute for Nuclear Research, Dubna. It uses the performances of CERN software GEANT 3.21 [42] with programming language FORTRAN 77 [43]. The *nemos* package includes also a complete set of specifications about the NEMO3 detector for all 20 sectors, 40 materials ( $\beta\beta$  isotopes, all kinds of background and materials used for the NEMO3 construction), and also about the different processes (different modes of  $\beta\beta$  decay, Möller scattering, Compton effect). Data evaluation and imaging was made with PAW 2.14 [44, 45, 46] and with the NEMO3 visualisation program developed at LAL Orsay [47]. All these programs are running under the Linux OS.

In summary, the NEMO3 simulation software includes:

- the NEMO3 geometry description;
- the generation of the initial kinematics of events;
- the transport of generated particles in the detector;
- the records of fired Geiger cells and scintillators, and their response to the generated particles;
- the graphical visualisation of events in the detector.

### 3.2 Trigger for Monte-Carlo simulations

Considering the randomization during the event simulation, some useless cases are also generated. Not to record them, the criteria under which an event will be recorded in the simulation output file were defined and they are the following:

- at least four Geiger cell layers closest to the source foils have to be fired;
- at least one scintillator counter has to be fired;
- if only one scintillator is fired, then the deposited energy has to be greater than 1300 keV;
- if more than one scintillator counter is fired, then the deposited energy in one of them has to be greater than 200 keV.

However, any user of the NEMO3 simulation program can freely modify such trigger according to his specific needs.

### 3.3 Types of simulated events

MC simulations play a very important role for understanding the processes which can occur in the detector and can influence the studied signal. This study is based mainly on the known activity values of the impurities inside the cadmium foils and of the detector filling gas, thus, several types of background were simulated.

The simulated processes are the following:

- $2\nu\beta\beta$  (g.s.  $\rightarrow$  g.s.) decay of  $^{116}\text{Cd}$ ;
- internal background of the cadmium source foils coming from  $^{228}\text{Ac}$ ,  $^{214}\text{Bi}$ ,  $^{40}\text{K}$ ,  $^{234m}\text{Pa}$ ,  $^{211}\text{Pb}$ ,  $^{207}\text{Tl}$ , and  $^{208}\text{Tl}$ ;
- radon contamination of the filling He gas of the detector.

The measured activity of impurities in the  $^{116}\text{Cd}$  source are listed in Table 2.4. The measured activity of radon inside of the detector is of  $30 \text{ mBq/m}^3$  [48]. On the basis of these values, the expected number of events for one year was estimated and then the appropriate number of events was generated (Table 3.1).

Isotope	Type of events	Number of generated events	Number of recorded events	Ratio rec./gen.
$^{116}\text{Cd}$	$2\nu\beta\beta$ (g.s. $\rightarrow$ g.s.)	$1 \times 10^6$	736,079	0.74
$^{228}\text{Ac}$	internal bg. (foil)	$1 \times 10^6$	434,331	0.42
$^{214}\text{Bi}$	internal bg. (foil)	$1 \times 10^6$	615,319	0.62
$^{40}\text{K}$	internal bg. (foil)	$1 \times 10^6$	446,533	0.45
$^{234m}\text{Pa}$	internal bg. (foil)	$1 \times 10^6$	660,024	0.66
$^{211}\text{Pb}$	internal bg. (foil)	$5 \times 10^5$	217,652	0.44
$^{207}\text{Tl}$	internal bg. (foil)	$5 \times 10^5$	235,463	0.47
$^{208}\text{Tl}$	internal bg. (foil)	$5 \times 10^5$	344,108	0.69
$^{214}\text{Bi}$	$^{222}\text{Rn}$ inside gas	$5 \times 10^6$	3,996,852	0.80

Table 3.1: List of simulated types of events with the numbers of generated and recorded events.

### 3.4 Definition of particles in Monte-Carlo events

In each data file, there are many events with different types of particles. To analyse them, it is necessary to find general rules to distinguish between electrons, positrons, photons, and  $\alpha$ -particles detected in NEMO3. As only two-electron events are searched for in the current analysis, and thanks to the cuts which will be described later, only electrons and  $\alpha$ -particles, which come from radon daughters, are taken here into account.

#### 3.4.1 Electrons

An electron is defined as a reconstructed track starting from the source foil, passing through the wire chamber and having a negative curvature with respect to the source foil. Furthermore, each track has associated scintillator (not necessarily the only one) in order to measure its energy. When two electrons from  $\beta\beta$  decay are searched for, except the mentioned criteria both electrons must have the same vertex inside the foils and must be emitted at the same time.

However, it is possible to find two tracks fulfilling the previous criteria, but in reality, there is one electron originating from the outside of the source foils which crosses through it. Thanks to miscellaneous processes mentioned in section 2.3, it can knock out the second electron from the foil. These cases bear on background and not on the  $\beta\beta$  signal. For their rejection, the TOF tests taking into

account the time evolution of the event tracks are used. Thus, the internal events can be distinguished from the external crossing events (see schemes in Figure 3.1). Examples of the  $\beta\beta$  events are given in Figure 3.2.

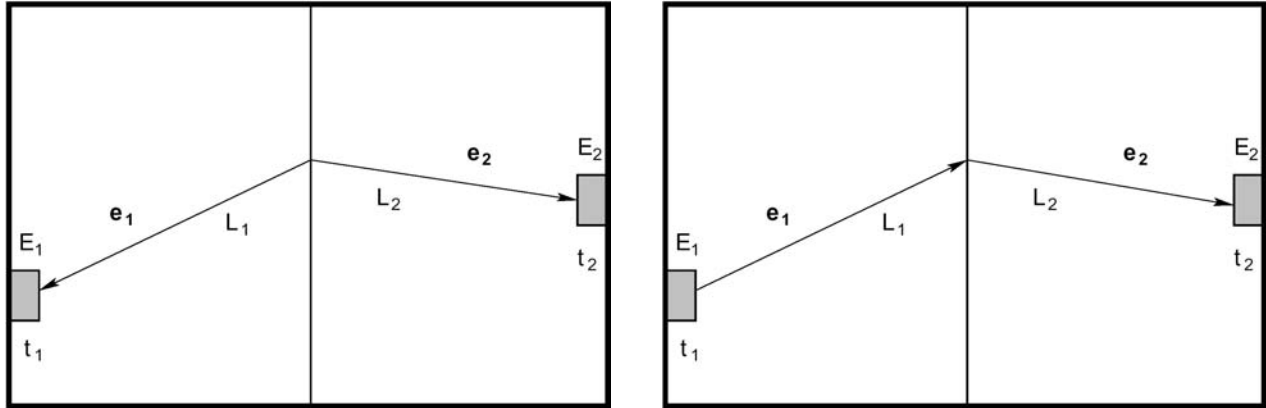


Figure 3.1: The possible scenarios of the two-electron events. Left: The internal event (two electrons emitted from the source foil). Right: The external event (an electron crossing through the wire chamber).

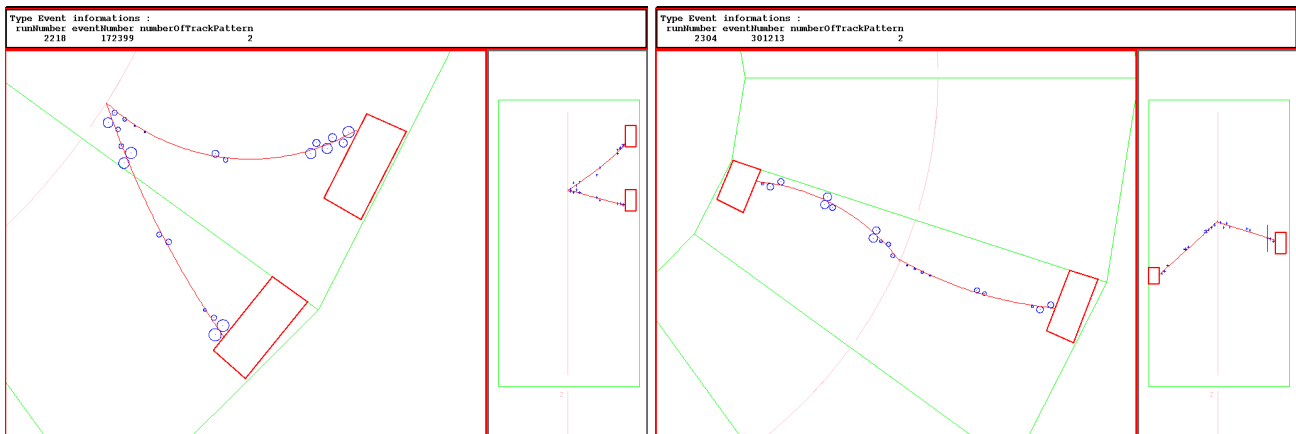


Figure 3.2: The examples of the  $\beta\beta$  decay events.

### 3.4.2 $\alpha$ -particles

$\alpha$ -particles are strongly-ionizing particles, thus, their tracks are characterized with several neighbouring fired Geiger cells. Moreover, these Geiger cells are characterized with a delay in comparison with electrons. The delayed Geiger cells can also occur, when the cell is re-fired with a short delay after an electron have passed close to it. In general, the delay is less than  $46 \mu\text{s}$ . This delay time is used as one of the selection criteria. Examples of the events with  $\alpha$ -particles are shown in Figure 3.3.

## 3.5 Construction of selection criteria

As previously mentioned, regarding their origin, there are two main kinds of background - internal and external. The internal background is caused by impurities inside of the source foils which can emit  $\alpha$ - and  $\beta$ -particles and also  $\gamma$ -rays. These particles can generate through different processes two electrons.

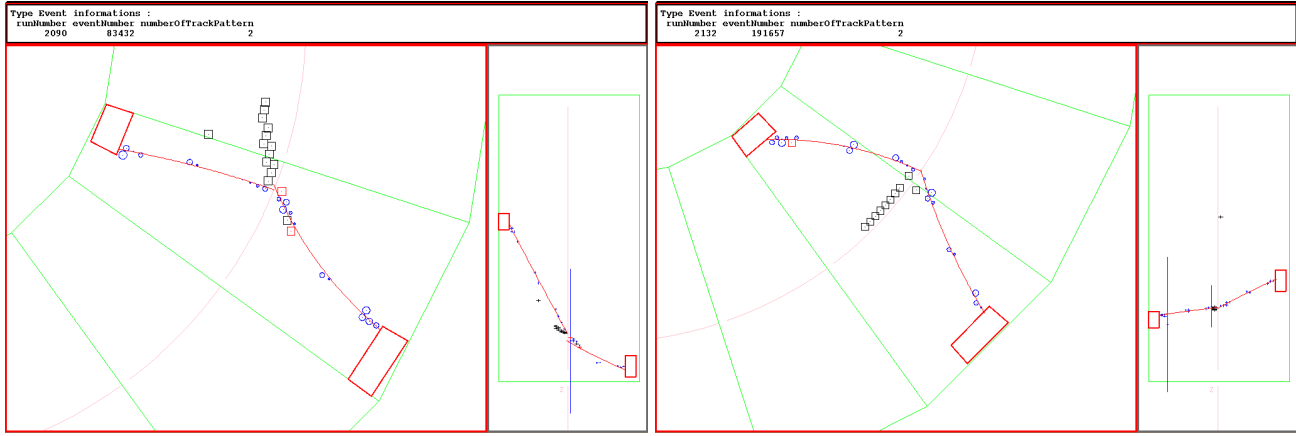


Figure 3.3: The examples of the  $\beta\beta$  decay events with  $\alpha$ -particle (black squares).

As these two electrons are emitted from the foil at the same moment, they mimic the signal events and, thus, they deform the statistics and the result.

One of the objectives of the analysis is to find the optimal selection criteria which will reduce all the types of background as much as possible, but which will only slightly reduce the signal. All the selection criteria used for analysis of the  $\beta\beta$  signal can be divided into two groups. The first group includes the topological criteria which ensue from the character of the study. For example, when one searches for the  $\beta\beta$  events, only two-electron tracks are selected. The other group of criteria is based on the study of simulations. They include, for example, the criteria for energies of electrons, or for the emission angle between electrons and they are generally defined on the basis of MC simulations of the signal and background.

The main characteristics of the simulated isotopes are summarized in Table 3.2.

Isotope	Relative mass ( $m_u$ )	$T_{1/2}^{2\nu\beta\beta}$	$J^P$	Decay mode	$Q_\beta$ (keV)	Activity (mBq/kg)	Decays for year
$^{116}\text{Cd}$	115.905	?	0+	$\beta\beta$ (100 %)	2809(4)		
$^{228}\text{Ac}$	228.031	6.15(2) h	3+	$\beta^-$ (100 %)	2127(3)	3.076	39,297
$^{214}\text{Bi}$	213.999	19.9(4) m	1-	$\beta^-$ (99.979(1) %) $\alpha$ (0.021(1) %)	3272(11) 5616.8(10)	1.608	20,540
$^{40}\text{K}$	39.964	$1.277(8)\times 10^9$ y	4-	$\beta^-$ (89.28(13) %) EC/ $\beta^+$ (10.72(13) %)	1311.09(12) 1504.9(3)	16.764	214,200
$^{234m}\text{Pa}$	234.043	1.17(3) m	(0-)	$\beta^-$ (99.84(4) %) IT (0.16(4) %), SF ( $j \cdot 10^{-9}$ )	2195(5)	35.662	455,655
$^{211}\text{Pb}$	210.989	36.1(2) m	9/2+	$\beta^-$ (100 %)	1372(6)	0.358	4,575
$^{207}\text{Tl}$	206.977	4.77(2) m	1/2+	$\beta^-$ (100 %)	1423(6)	0.411	5,249
$^{208}\text{Tl}$	207.982	3.053(4) m	5(+)	$\beta^-$ (100 %)	5001.0(17)	0.677	8,656
$^{214}\text{Bi}$ (Radon, gas volume $\approx 27 \text{ m}^3$ )						30 mBq/m <sup>3</sup>	25,561,100

Table 3.2: The simulated isotope characteristics. Ref. [12, 17, 32].

### 3.5.1 Topological and time-of-flight cuts

To select good two-electron events of  $^{116}\text{Cd}$  double beta decay, the only events which contain two reconstructed tracks are selected. These tracks with negative curvature must have a common vertex inside the cadmium source foil. Each track is associated to a different scintillator. To ensure that the  $\beta$ -particle originates in the foil, the Geiger cells which are close to the source foil must be fired. Both

tracks end in the two last layers close to the scintillators. The cases when tracks start from inside of the plexiglass strip support or from the copper tube are rejected.

To distinguish between the internal and external event, the TOF criteria are applied. For each event, the probabilities of hypothesis that such event is of the internal  $P_{int}$  or of the external  $P_{ext}$  type are evaluated. The good internal event has to satisfy  $P_{int} \geq 10^{-2}$  and  $P_{ext} \leq 10^{-3}$ . Both values were determined on the basis of the previous MC studies [32, 33].

### 3.5.2 Electron energy cuts

One of the possible ways of the background reduction are cuts on the minimal and maximal energy of electrons. With respect to the single-electron spectrum shape (Figure 3.4), main emphasis was laid on limitation of the minimal energy in the first half of the spectrum. The restriction of the energies in the second half is not so effective because of the fast decrease of the useful signal towards the higher energies.

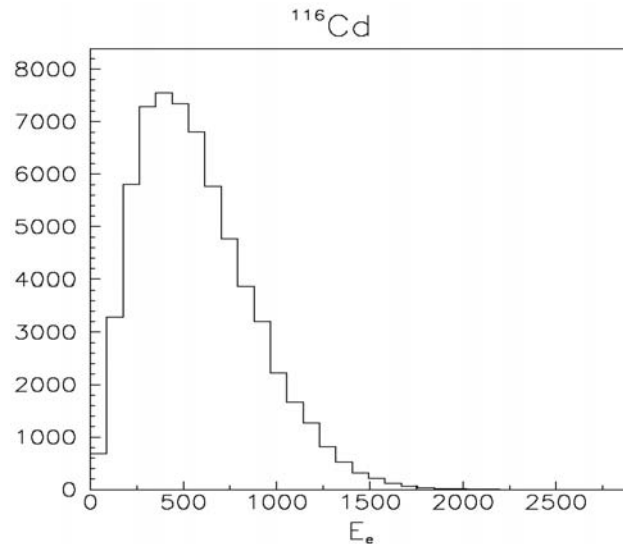


Figure 3.4: The single-electron energy spectrum for simulated events from  $^{116}\text{Cd}$ .

During analysis of the two-electron events, electrons are divided by their energy to those with lower energy,  $E_{min}$ , and to those with higher energy,  $E_{max}$ . Figures 3.5 and 3.6 show the energy spectra of simulated isotopes for electrons with lower  $E_{min}$  (blue histograms) and higher  $E_{max}$  (red histograms) energy and their total energy  $E_{tot}$  ( $E_{tot} = E_{min} + E_{max}$ ). It is evident, that with a certain combination of energy cuts for each electron, several background isotopes ( $^{40}\text{K}$ ,  $^{207}\text{Tl}$ ,  $^{211}\text{Pb}$ ) can be rejected completely thanks to their low  $Q_{\beta\beta}$  value. Yet, there are also isotopes having very wide spectra ( $^{214}\text{Bi}$ ,  $^{234m}\text{Pa}$ ,  $^{208}\text{Tl}$ ) which can be reduced only partially. However, there exist a limit for the minimal energy of both electrons which is about the maximum of the  $\beta\beta$  spectrum ( $\approx Q_{\beta\beta}/3$ ). The overlap of this value increases the signal/background ratio but radically decrease the number of signal events and, thus, decrease the statistics. However, there exists a discrimination level for single-electron energy at 200 keV, fixed by scintillators and tracking device to obtain acceptable resolution. Thus, the sum energy of both electrons,  $E_{tot}$ , should be at least 400 keV.

The main indicator of the condition quality is the ratio of the expected signal vs. background events given, for example, for one year. At the same time, the number of expected events for one year was also watched in order it may not to be too small. The expected number of decays,  $N_{dec}$ , and the expected number of selected events,  $N_{sel}$ , after the application of cuts are calculated in the following way:

$$N_{dec} = A \times t, \quad (3.1)$$

$$N_{sel} = A \times t \times \varepsilon, \quad (3.2)$$

where  $A$  stands for the activity of a considered isotope,  $t$  is the time of measurement, and  $\varepsilon$  represents the efficiency of the applied set of selection criteria and is equal to the ratio of number of selected and simulated events. The results of computations are listed in Table 3.3 where the different values of  $E_{min}$  and  $E_{max}$  are listed together with the corresponding signal/background ratios. Signal and background were both normalized for the same time period of one year.

$E_{min}/E_{max}$	Sig./1yr	Sig./Bg.	$E_{min}/E_{max}$	Sig./1yr	Sig./Bg.	$E_{min}/E_{max}$	Sig./1yr	Sig./Bg.
200/200	1988.56	4.54	300/300	1513.32	4.98	400/500	970.39	5.00
200/300	1966.08	4.55	300/400	1475.17	4.98	400/600	858.01	5.30
200/400	1868.67	4.64	300/500	1354.93	4.95	400/700	691.96	6.22
200/500	1685.45	4.68	300/600	1165.20	5.28	400/800	518.83	6.26
200/600	1432.43	4.99	<b>300/700</b>	<b>928.39</b>	<b>5.98</b>	500/500	601.25	4.93
200/700	1139.60	5.61	300/800	693.42	7.20	500/600	564.95	5.09
200/800	853.97	6.24	400/400	1011.47	5.04	500/700	472.20	6.24

Table 3.3: S/B ratios together with expected number of signal events after 1 year for different limits on  $E_{min}$  and  $E_{max}$ .

As optimal cuts with more than five-times higher signal over background and corresponding still to relatively high number of signal events seems to be conditions demanding that the low energy electron has energy  $E_{min} \geq 300$  keV and the high energy electron satisfies  $E_{max} \geq 700$  keV.

Another cut possibility was studied when the sum energy of electrons,  $E_{tot}$ , was restricted from below in different ways, but this kind of cuts was not so effective and only caused the decrease of the signal/background ratio.

In the same way as for  $E_{min}$  and  $E_{max}$ , a criterion for the sum energy restricted from above was studied; the previous selected energy cuts have already been taken into account. The results are given in Table 3.4. The optimal cut was determined as  $E_{tot} \leq 2200$  keV.

$E_{tot}$	Sig./1yr	Sig./Bg.	$E_{tot}$	Sig./1yr	Sig./Bg.	$E_{tot}$	Sig./1yr	Sig./Bg.
< 2810	928.39	6.03	<b>&lt; 2200</b>	<b>921.96</b>	<b>6.27</b>	< 1600	650.28	6.33
< 2700	928.39	6.04	< 2100	913.87	6.26	< 1500	528.77	5.87
< 2600	928.31	6.05	< 2000	894.78	6.15	< 1400	388.02	6.34
< 2500	928.08	6.05	< 1900	864.26	6.04	< 1300	240.09	6.13
< 2400	927.52	6.06	< 1800	816.85	6.21	< 1200	116.74	6.13
< 2300	925.85	6.08	< 1700	745.01	7.41	< 1100	31.23	5.12

Table 3.4: S/B ratios together with expected number of signal events after 1 year for different limits on  $E_{tot}$ .

The expected values for signal and each background contribution for the case of the basic cuts ( $E_{min} \geq 200$  keV,  $E_{max} \geq 200$  keV) and for the optimal case ( $E_{min} \geq 300$  keV,  $E_{max} \geq 700$  keV,  $E_{tot} \leq 2200$  keV) are compared in Table 3.5.

### 3.5.3 Angle between the emitted electrons

Similar study as in the case of energy cuts was realized in order to determine the optimal selection criterion for the angle  $\theta$  between two emitted electrons exiting the source foil. Its determination is

Isotope	Basic energy cuts $E_{min, max} \geq 200$ keV			$E_{min} \geq 300$ keV, $E_{max} \geq 700$ keV, $E_{tot} \leq 2200$ keV		
	Selected event number	Efficiency $\epsilon$	Expected after 1 yr	Selected event number	Efficiency $\epsilon$	Expected after 1 yr
$^{116}\text{Cd}$	51,651	$5.17 \times 10^{-2}$	1,988.56	23,947	$2.40 \times 10^{-2}$	921.96
$^{228}\text{Ac}$	473	$4.73 \times 10^{-4}$	18.59	174	$1.74 \times 10^{-4}$	6.84
$^{214}\text{Bi}$	984	$9.84 \times 10^{-4}$	20.21	487	$4.87 \times 10^{-4}$	10.00
$^{40}\text{K}$	88	$8.80 \times 10^{-5}$	18.85	0	0.00	0.00
$^{234m}\text{Pa}$	735	$7.35 \times 10^{-4}$	334.91	256	$2.56 \times 10^{-4}$	116.65
$^{211}\text{Pb}$	55	$1.10 \times 10^{-4}$	0.50	1	$2.00 \times 10^{-6}$	0.01
$^{207}\text{Tl}$	41	$8.20 \times 10^{-5}$	0.43	2	$4.00 \times 10^{-6}$	0.02
$^{208}\text{Tl}$	511	$1.02 \times 10^{-3}$	8.85	185	$3.70 \times 10^{-4}$	3.20
$^{214}\text{Bi}$ (Radon)	7	$1.40 \times 10^{-6}$	35.79	2	$4.00 \times 10^{-7}$	10.22

Table 3.5: The influence of energy cuts on the number of selected events. The number of selected events with corresponding cut efficiency, and the expected number of events for one year are given for the basic cut and for the optimal case of cuts.

possible thanks to the 3D track reconstruction of the wire chamber. The distributions of  $\cos \theta$  for the simulated isotopes are given in Figure 3.7. One of the main meaning of this cut is the rejection of two-electron events caused by Möller scattering where the distribution is characterized by small angle between two electrons dominates while in the case of the signal the bigger angles (greater than  $\pi/2$ ) are dominant.

Also in this case, several intervals of angles were examined. At the same time, the previously defined energy cuts have been used. As an optimal interval, the one, which influence on background was significant but did not reduce the signal too much, was selected. The results are summarized in Table 3.6.

$\cos(\theta)$	Sig./1yr	Sig./Bg.	$\cos(\theta)$	Sig./1yr	Sig./Bg.	$\cos(\theta)$	Sig./1yr	Sig./Bg.
$\langle -1, 1.0 \rangle$	921.96	6.27	<b><math>\langle -1, 0.6 \rangle</math></b>	<b>797.22</b>	<b>7.31</b>	$\langle -1, 0.2 \rangle$	666.44	8.42
$\langle -1, 0.9 \rangle$	905.98	6.38	$\langle -1, 0.5 \rangle$	762.38	7.60	$\langle -1, 0.1 \rangle$	638.37	8.55
$\langle -1, 0.8 \rangle$	872.76	6.39	$\langle -1, 0.4 \rangle$	727.57	7.51	$\langle -1, 0.0 \rangle$	608.99	8.53
$\langle -1, 0.7 \rangle$	834.76	6.55	$\langle -1, 0.3 \rangle$	696.12	7.85	$\langle -1, -0.1 \rangle$	578.46	8.81

Table 3.6: The optimal electron emission angle estimation.

As the optimal angle-interval was chosen  $\cos \theta \in \langle -1, 0.6 \rangle$ . It also improved the signal/background ratio but the decrease in the number of expected signal events is not too big (Table 3.7).

### 3.6 Final set of the cuts for two-electron search

In this section, the complete set of cuts used for analysis of the NEMO3 data will be summarized. The basic idea for searching for the  $2\nu\beta\beta$  decay process is that good two-electron internal events are needed. Furthermore, additional cuts are used to suppress the undesirable background events and to enhance the measured signal.

All good events have to satisfy the following conditions:

- Topological cuts
  - decay vertex is inside of the  $^{116}\text{Cd}$  foils;
  - vertex of each track is not inside the plexiglass strip support;
  - vertex of a track is not inside the copper tube;

Isotope	No emission angle cut			$\cos \theta \in (-1, 0.6)$		
	Selected event number	Efficiency $\varepsilon$	Expected after 1 yr	Selected event number	Efficiency $\varepsilon$	Expected after 1 yr
$^{116}\text{Cd}$	23,947	$2.411 \times 10^{-2}$	928.39	20,707	$2.07 \times 10^{-2}$	797.22
$^{228}\text{Ac}$	174	$1.740 \times 10^{-4}$	6.84	135	$1.35 \times 10^{-4}$	5.31
$^{214}\text{Bi}$	487	$6.050 \times 10^{-4}$	12.43	390	$3.90 \times 10^{-4}$	8.01
$^{40}\text{K}$	0	0.000	0.00	0	0.00	0.00
$^{234m}\text{Pa}$	256	$2.560 \times 10^{-4}$	116.65	193	$1.93 \times 10^{-2}$	87.94
$^{211}\text{Pb}$	1	$2.000 \times 10^{-6}$	0.01	0	0.00	0.00
$^{207}\text{Tl}$	2	$4.000 \times 10^{-6}$	0.02	2	$4.00 \times 10^{-6}$	0.02
$^{208}\text{Tl}$	185	$4.540 \times 10^{-4}$	3.93	157	$3.14 \times 10^{-4}$	2.72
$^{214}\text{Bi}$ (Radon)	2	$4.000 \times 10^{-7}$	10.22	1	$2.00 \times 10^{-7}$	5.11

Table 3.7: The influence of the angle cut on the number of selected events. The selected event number with corresponding cut efficiency, and the expected number of events for one year are listed for no angular cut case and for the final set of cuts.

- number of reconstructed tracks is equal to two;
  - there are only two fired scintillators in the event;
  - each track is associated with a fired scintillator;
  - only two electrons are selected, i. e. both tracks have negative curvature;
  - both tracks have a common vertex with  $|\Delta(x, y)| \leq 4 \text{ cm}$ ,  $|\Delta z| \leq 4 \text{ cm}$ ;
  - each track is associated with a different scintillator;
  - each track starts from the first layers of Geiger cells close to the foil;
  - each track ends in the two last layers of Geiger cells close to scintillators.
- TOF cuts
    - the event is of the internal character, crossing event is rejected;  $P_{int} \geq 10^{-2}$  and  $P_{ext} \leq 10^{-3}$ .
  - Energy cuts
    - low-energy electron deposits in scintillator satisfies  $E_{min} \geq 300 \text{ keV}$ ;
    - high-energy electron deposits energy satisfies  $E_{max} \geq 700 \text{ keV}$ ;
    - sum energy of both electrons is  $E_{tot} \leq 2200 \text{ keV}$ .
  - Angular cuts
    - the emission angle between two electrons satisfies  $\cos \theta \leq 0.6$ .
  - $\alpha$ -particle cuts
    - no reconstructed alpha track is present in the event;
    - there is no Geiger cell hit caused by  $\alpha$ -particle near the two-electron vertex ( $|\Delta(x, y)| \leq 10 \text{ cm}$ ,  $|\Delta z| \leq 20 \text{ cm}$ ) with delay greater than  $46 \mu\text{s}$ ;
    - if the event contains only 2 delayed Geiger cells near the vertex, they are separated in time by more than  $1.5 \mu\text{s}$ ;
    - if the event contains at least two Geiger cell hits in time which are near the vertex ( $|\Delta(x, y)| \leq 20 \text{ cm}$ ,  $|\Delta z| \leq 20 \text{ cm}$ ) and which are not associated to any of the tracks, the event is rejected.

Although this analysis method rejects the  $ee\alpha$  events, they are used for radon background study based on experimental data where, on contrary, the  $\alpha$ -particles near the vertex are looked for.

After applying these cuts, the expected number of signal events is 797.22/yr, the expected number of background events 109.11/yr, and the signal/background ratio is 7.31.

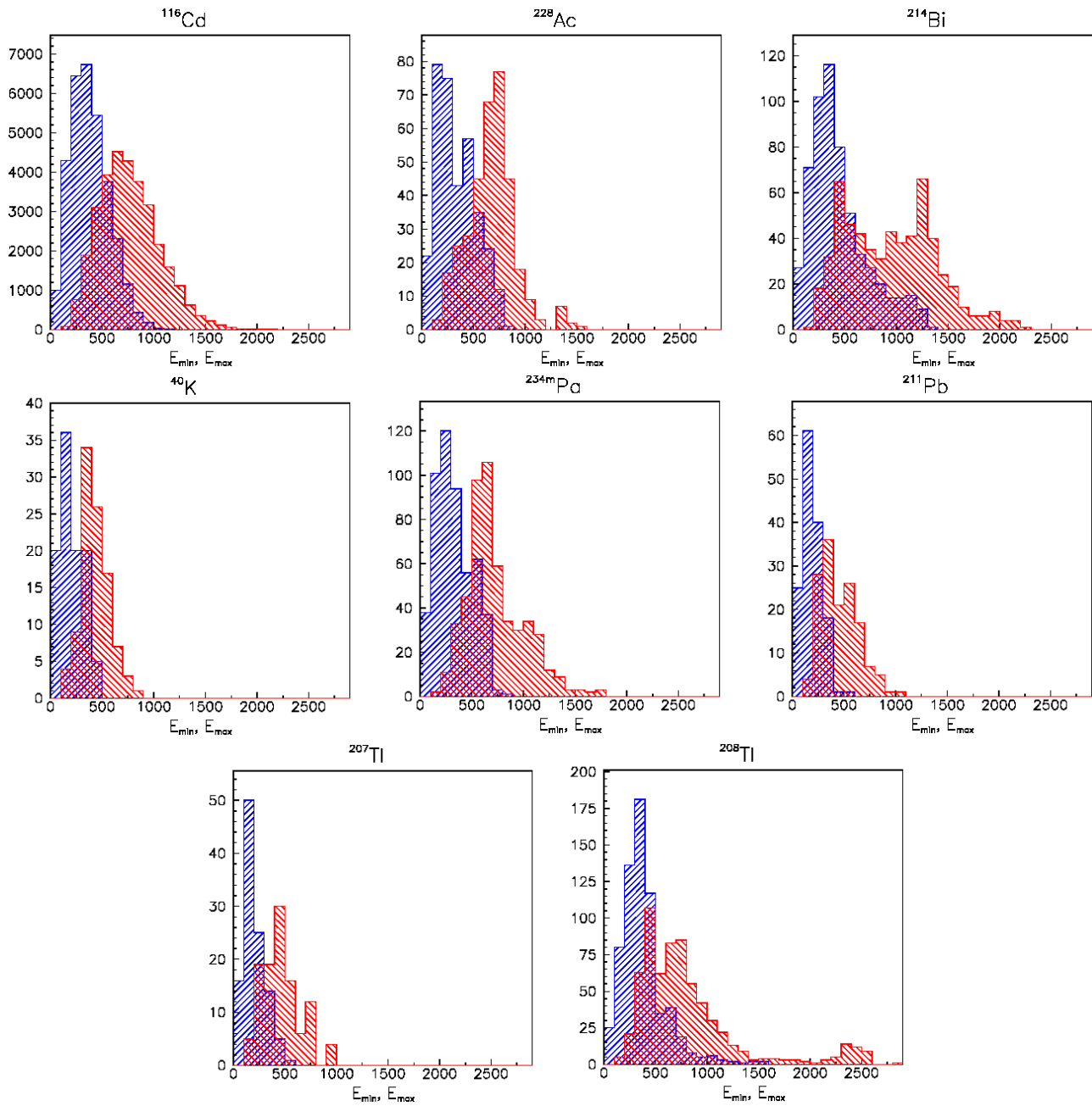


Figure 3.5: The single-electron energy spectra for simulated isotopes. The blue histograms correspond to spectra of low-energy electrons ( $E_{min}$ ) while the red histograms represent spectra of high-energy electrons ( $E_{max}$ ).

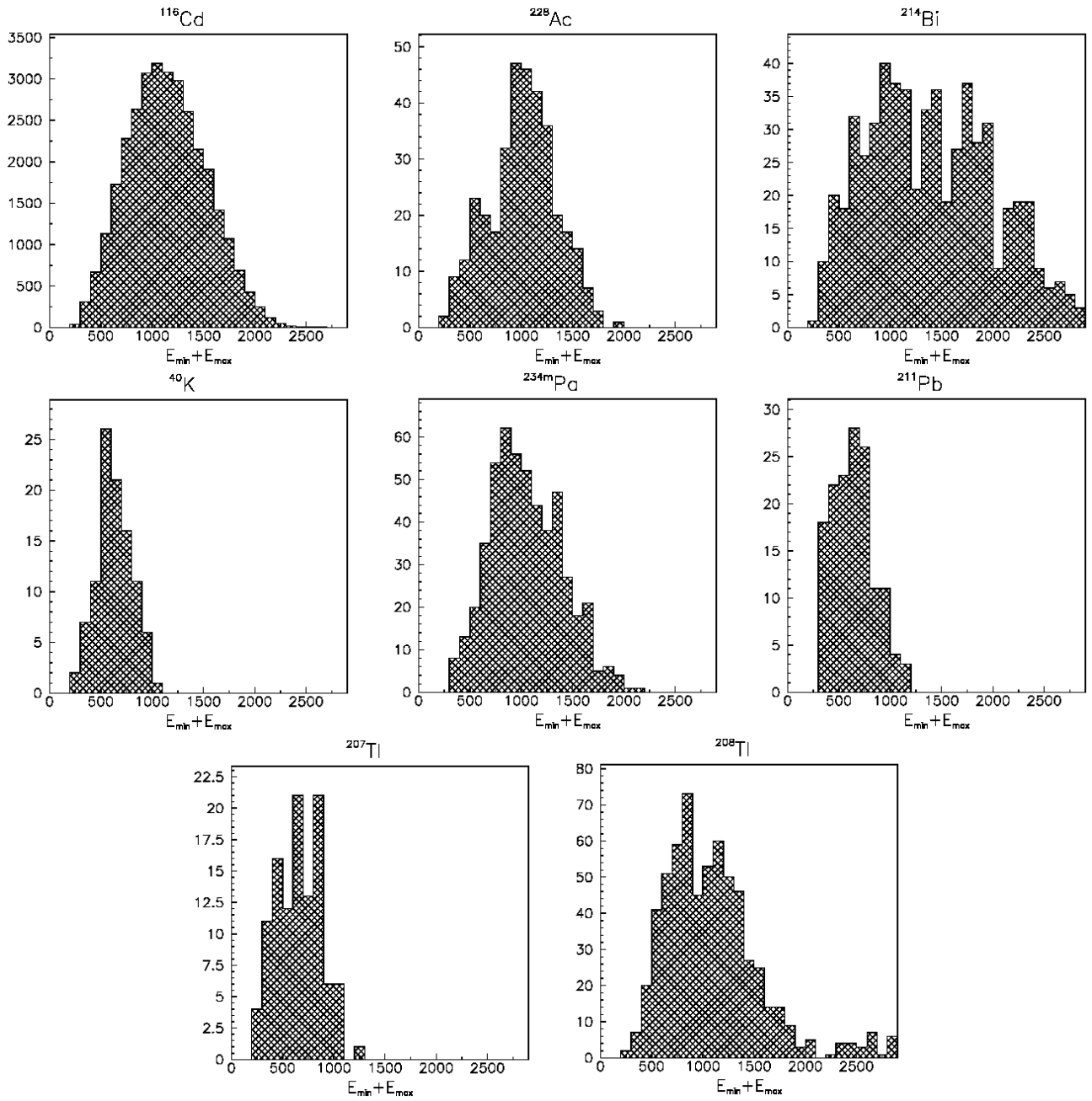


Figure 3.6: The total two-electron energy spectra ( $E_{tot}$ ) for simulated isotopes.

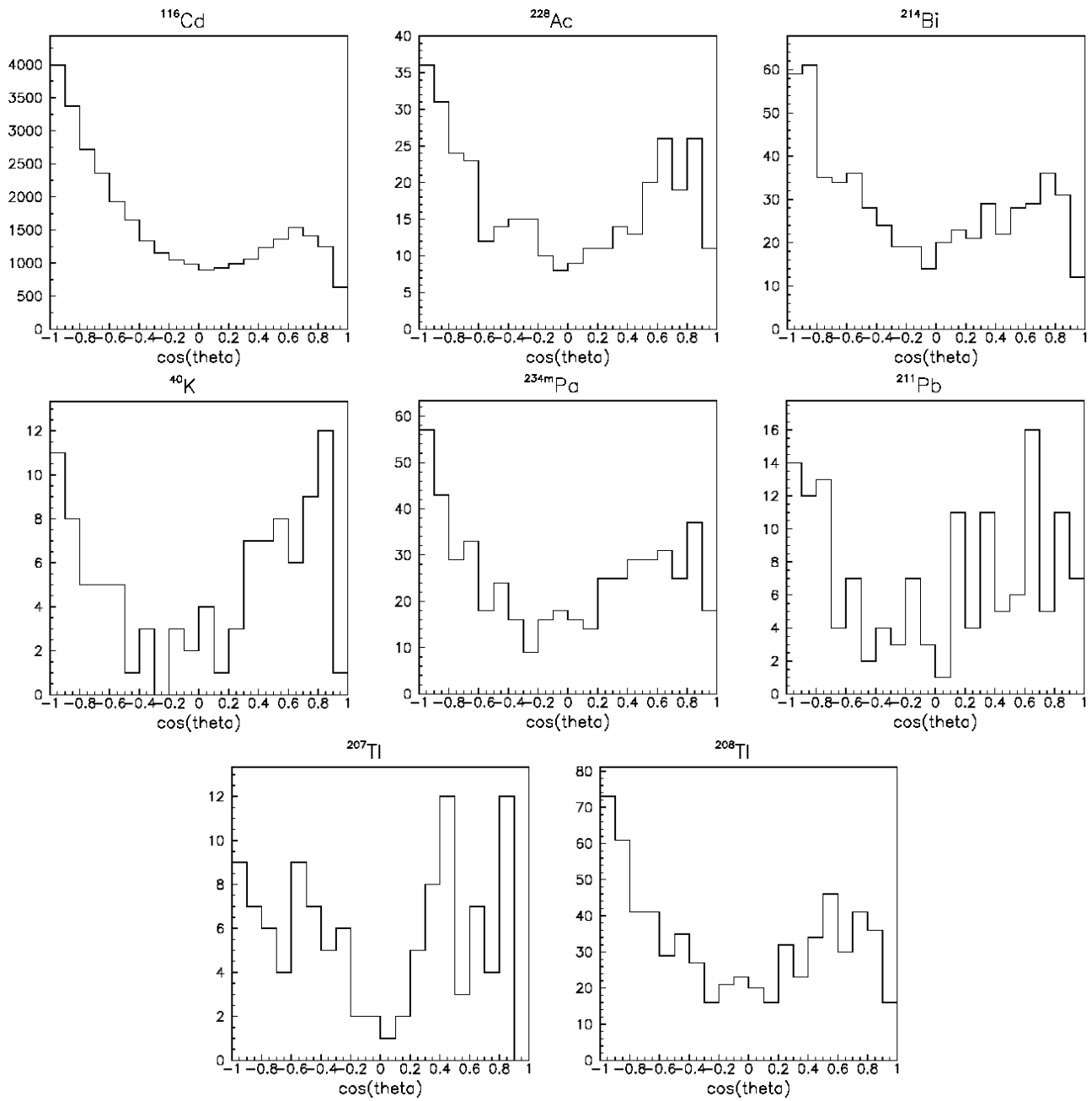


Figure 3.7: Angular distribution of the two emitted electrons for different simulated isotopes.

# Chapter 4

## Data analysis

### 4.1 Software tools for the data analysis

Data from the NEMO3 experiment are recorded in n-tuples in the raw data format. These files contain the following information:

- general run and event information: number and date of the run, number of recorded events, number and time of each event;
- calorimeter data: number of triggered scintillators, their location in the detector, and the ADC and TDC contents of corresponding PMTs;
- wire chamber data: number of fired Geiger cells, their location, and the corresponding TDC contents for the anodic and both top and bottom cathodic signals, as well as contents of slow TDCs.

These raw data are not used directly for the analysis. They are reprocessed into the so-called analysis format which n-tuples contain more information calculated on the basis of the raw data and the NEMO3 calibration database. This is done by the pre-analysis program *anal.exe* [47] which was developed in LAL Orsay. This program communicates with the NEMO3 calibration database [49] in order to obtain the calibration and correction data. Besides all the variables of the raw data format, data in the analysis format include also the following information:

- energies and times with corresponding errors for fired scintillator counters recalculated from the TDC and ADC contents;
- reconstructed positions of charge particle passage and corresponding errors;
- further tracking information such as number of reconstructed tracks in the event, the track length, information about the starting and ending points of tracks, position of reconstructed vertex, ID of scintillator associated to the track if any, the corresponding impact point in scintillator, and information about the curvature and fit parameters;
- $\alpha$  tracking information if the  $\alpha$ -track was reconstructed from delayed Geiger cells.

Then the data are analysed with use of PAW program and FORTRAN routines containing the selection criteria and other scripts for generating of histograms, plotting spectra, computation of different variables and so on. Data visualisation was also made with PAW and with the NEMO3 visualisation program.

## 4.2 Analyzed runs

The runs collected during the year 2003 were used for the analysis presented in this work. In particular, only good runs corresponding to the run status equal to 1 were selected. The run status [50] is used for the evaluation of the conditions and quality of each run. For example: status 0 = bad run, unusable for analysis, 1 = good run, 1000 = less than 24 hours after calibration runs, 100000 = ventilation off, high radon rate, and so on. The detail information about the used runs are summarized in the Table 4.1.

Period	Number of runs	Time (hh:mm:ss)	Recorded events
February 2003	43	282:05:11	7,548,673
March 2003	44	281:25:19	7,579,614
April 2003	38	377:38:34	10,435,709
May 2003	78	609:11:14	16,782,952
June 2003	42	404:53:36	12,156,666
July 2003	47	544:32:33	15,860,261
August 2003	55	562:39:25	15,596,944
September 2003	48	432:48:07	11,899,163
October 2003	23	128:27:09	3,653,923
November 2003	54	417:22:57	10,806,597
December 2003	54	421:29:22	11,097,439
Sum	526	4462:29:27	123,417,941

Table 4.1: Summary of analysed runs. For each month, the number of used runs, the total acquisition time, and the number of recorded events are given.

All the analysed files were transformed into the analysis format. The selection criteria defined in section 3.6 for the measurement of the  $2\nu\beta\beta$  decay of  $^{116}\text{Cd}$  were applied on them. After the summation of the selected events (Table 4.2) which fulfilled all the selection criteria. The background contribution was estimated from MC simulations. Knowing the acquisition time, source activities (Table 2.4), and the efficiency  $\varepsilon$  of the considered channel (Table 3.7), the expected number of background events was determined (eq. 3.2). The number of expected background events corresponding to 4462.5 hours of collected data are summarized in Table 4.3.

Period	Selected events	Period	Selected events
February 2003	25	August 2003	50
March 2003	26	September 2003	56
April 2003	53	October 2003	11
May 2003	66	November 2003	49
June 2003	36	December 2003	58
July 2003	54	Sum	484

Table 4.2: The number of selected events for each month.

Now, the background contribution can be subtracted from the total number of selected events in order to get the number of signal events from the  $2\nu\beta\beta$  decay of  $^{116}\text{Cd}$ . Then, knowing the time of data collection and the number of signal events, the  $2\nu\beta\beta$  decay half-life of  $^{116}\text{Cd}$  can be evaluated. The half-life value,  $T_{1/2}$ , can be determined from the radioactivity decay law in the following way using approximation for  $\lambda \rightarrow 0$ :

$$\Delta N = \varepsilon N_0(1 - e^{-\lambda t}) \approx \varepsilon N_0 \lambda t = \varepsilon \frac{N_A}{A} m \frac{\ln 2}{T_{1/2}} t \Rightarrow T_{1/2} = \varepsilon \frac{N_A}{A} m \frac{\ln 2}{\Delta N} t, \quad (4.1)$$

Isotope	Expectation for 4462.5 h	Isotope	Expectation for 4462.5 h
$^{228}\text{Ac}$	2.70	$^{211}\text{Pb}$	0.00
$^{214}\text{Bi}$	4.07	$^{207}\text{Tl}$	0.01
$^{40}\text{K}$	0.00	$^{208}\text{Tl}$	1.38
$^{234m}\text{Pa}$	44.77	$^{214}\text{Bi}$ (Radon)	2.60
Background Sum: 55.53 events for 4462.5 hours			

Table 4.3: The expected number of background events determined from MC simulations for the considered acquisition period.

where  $\Delta N$  is the number of registered decays,  $N_0$  is the initial number of atoms at  $t = 0$ ,  $t$  is the observation time,  $\lambda$  is the decay constant,  $N_A$  is the Avogadro constant,  $A$  is the mass number of the atom,  $m$  is the mass of the observed isotope, and  $\varepsilon$  is the efficiency of detection. For  $^{116}\text{Cd}$ , the mass number is  $A = 115.90$  and the sample mass is  $m = 404.89$  g.

The resulting half-life value obtained after background subtraction is:

$$T_{1/2}^{2\nu\beta\beta} (^{116}\text{Cd}) = [3.70 \pm 0.24(\text{stat.}) \pm 0.26(\text{syst.})] \times 10^{19} \text{ yr.}$$

Here, the systematic error is evaluated by the NEMO Collaboration to be 7 % [51]. It is caused, on one hand, by uncertainties originating from the MC simulations, on the other hand, there is a contribution from the measurement of foil impurity activities.

The obtained result is in a good agreement with the one of NEMO2 experiment [21]. Within the error bounds, it is also in agreement with the other values [20, 22, 23]. As the background was obtained only on the basis of the values of measured activities and was not measured directly, the error in determination of background can be in reality greater.

The possible modifications which would improve the current result consist in more stringent cuts, in the estimation of background directly from experimental data, in increasing of the statistics with data collected during year 2004, and with radon background reduction (anti-radon device in the LSM laboratory).



# Conclusion

NEMO3 is one of the several currently running experiments which investigate the double beta decay. Its great effort is aimed to neutrinoless double beta decay of  $^{100}\text{Mo}$  and  $^{82}\text{Se}$  but also  $^{116}\text{Cd}$  can be investigated. The subject of this research work is the analysis of  $^{116}\text{Cd}$  data which were collected during the year 2003 by this experiment.

The first half of the research work depicts the basic ideas about double beta decay and the methods of its measurement together with some details about the isotope  $^{116}\text{Cd}$ . Mainly the description of the NEMO3 experiment, its principal components as the tracking wire chamber, calorimeter, source foils, background, and the ways of its reduction, are treated in more detail; also the previous technical prototypes are mentioned.

The second half of this work is dedicated to the analysis of data. The method of determination of the  $^{116}\text{Cd}$  half-life is based mainly on knowledge of background contributions appearing from the inside of the cadmium foils but also from the detector wire chamber filling gas impurities. It is based on Monte-Carlo simulations which are very useful for construction and setting the selection criteria to look for the proper decay mode. In particular, the energy and angular cuts were developed on the basis of Monte-Carlo simulations. After that, these cuts were applied on data from February to December 2003. The obtained result of the two-neutrino double beta decay half-life for  $^{116}\text{Cd}$  is:

$$T_{1/2}^{2\nu\beta\beta} (^{116}\text{Cd}) = [3.70 \pm 0.24(\text{stat.}) \pm 0.26(\text{syst.})] \times 10^{19} \text{ yr.}$$

This value is in a good agreement with the other experiments, in particular with the NEMO2 result.

As the data will be collected in NEMO3 up to the year 2008 and thanks to building the anti-radon device during the autumn 2004, which will suppress the external background from radon by a factor of about 50, this value will be improved. Also study of other decay modes of  $^{116}\text{Cd}$  will be then possible.



# References

- [1] T. Tomoda, Rep. Prog. Phys. **54** (1991) 53.
- [2] A. Faessler and F. Šimkovic, J. Phys. G **24** (1998) 2139.
- [3] S.R. Elliott and P. Vogel, Annu. Rev. Nucl. Part. Sci. **52** (2002) 115; hep-ph/0202264.
- [4] M. Doi and T. Kotani, Prog. Theor. Phys. **87** (1992) 1207.
- [5] M. Doi and T. Kotani, Prog. Theor. Phys. **89** (1993) 139.
- [6] E. Kh. Akhmedov, *lectures given at Trieste Summer School in Particle Physics, June 7 – July 9, 1999*; arXiv:hep-ph/0001264, 2000.
- [7] P. Vogel, Phys.Rev. **D64** (2001) 054009; arXiv:nucl-th/0005020.
- [8] K. Zuber, Phys.Rept. **305** (1998) 295-364; arXiv:hep-ph/9811267.
- [9] M. Goepfert-Mayer, Phys. Rev. **48**, 512-16 (1935).
- [10] W. Fury, Phys. Rev. **56**, 1184 (1939).
- [11] A. S. Barabash (NEMO Collaboration), Czech. J. Phys. **52** (2002) 567-581.
- [12] *WWW Table of Radioactive Isotopes*, <http://ie.lbl.gov/toi/nucSearch.asp>.
- [13] *Campus program.com Pages*, <http://www.campusprogram.com/reference/en/wikipedia/c/ca/cadmium.html>.
- [14] *Jefferson Lab Pages*, <http://education.jlab.org/itselemental/ele048.html>.
- [15] F. W. Aston, Proc. Roy. Soc. **A149**, 396 (1935).
- [16] A. O. Nier, Phys. Rev. **50**, 10411045 (1936).
- [17] R. B. Firestone, *WWW Table of Atomic Masses*, <http://ie.lbl.gov/toi2003/MassSearch.asp>.
- [18] R. G. Winter, Phys. Rev. **99**, 8892 (1955).
- [19] L. W. Mitchell and P. H. Fisher, Phys. Rev. C **38**, 895899 (1988).
- [20] H. Ejiri *et al.* (ELEGANT Collaboration), J. Phys. Soc. of Japan **64** (1995) 339.
- [21] R. Arnold *et al.* (NEMO Collaboration), Z. Phys. C **72** (1996) 239.
- [22] F. A. Danevich *et al.* (SOLOTVINA Collaboration), Phys. Rev. C **68**, 035501 (2003).
- [23] Yu. Shitov (NEMO Collaboration), contribution to the XXXIXth Rencontres de Moriond EW 2004 conference; arXiv:nucl-ex/0405030, 2004.

- [24] D. Dassie *et al.* (NEMO Collaboration), Nucl. Instr. and Meth. **A309** (1991) 465-475.
- [25] NEMO Collaboration, *NEMO, Proposition d'expérience de double désintégration bêta pour la recherche d'une masse de neutrino de Majorana de 0.1 eV.*, Internal report, 1993.
- [26] R. Arnold *et al.* (NEMO Collaboration), Nucl. Inst. Meth. **A354** (1995) 338.
- [27] R. Arnold *et al.* (NEMO Collaboration), Nucl. Inst. Meth. **A401** (1997) 144.
- [28] R. Arnold *et al.* (NEMO Collaboration), Nucl. Phys. **A636** (1998) 209.
- [29] R. Arnold *et al.* (NEMO Collaboration), Nucl. Phys. **A658** (1999) 299.
- [30] D. Dassie *et al.* (NEMO Collaboration), Phys. Rev. **D51** (1995) 2090.
- [31] R. Arnold *et al.* (NEMO Collaboration), Z. Phys. **C72** (1996) 239.
- [32] R. Arnold *et al.* (NEMO Collaboration), *preprint submitted to Nucl. Instrum. Methods A*; [arXiv:physics/0402115](https://arxiv.org/abs/physics/0402115).
- [33] L. Vála (NEMO Collaboration), PhD thesis, Université Paris XI, 2003.
- [34] C. Jollet (NEMO Collaboration), PhD thesis, Université Paris VII, 2001.
- [35] R. Arnold *et al.* (NEMO Collaboration), Nucl. Inst. Meth. **A474** (2001) 93.
- [36] H. Ohsumi *et al.* (NEMO Collaboration), Nucl. Inst. Meth. **A482** (2002) 832.
- [37] C. Marquet *et al.* (NEMO Collaboration), Nucl. Inst. Meth. **A457** (2001) 487.
- [38] C. Berger *et al.*, Nucl. Instr. and Meth. **A262** (1987) 463.
- [39] G.T. Ewen, Nucl. Instr. and Meth. **A314** (1992) 373.
- [40] F. Mauger (NEMO Collaboration), *The NEMO3 Trigger Documentation*, Internal NEMO note, LPC Caen, 2001.
- [41] R. Arnold and V.I. Tretiak (NEMO Collaboration), *NEMO3 simulation program – Users guide*, NEMO note IReS-1/2001, December 2001.
- [42] *GEANT – Detector description and simulation tool*, CERN Program Library Long Writeup W5013, CERN, 1994.
- [43] C. G. Page, *Professional Programmers Guide to Fortran77*, <http://www.cmp.liv.ac.uk/docs/prof77.pdf>, University of Leicester, UK, 1995.
- [44] P. Juillot, *Introduction to PAW*, [http://ireswww.in2p3.fr/ires/recherche/cms/intro\\_paw.pdf](http://ireswww.in2p3.fr/ires/recherche/cms/intro_paw.pdf), IReS, Strasbourg, and CERN, Geneva, Switzerland, 2003.
- [45] O. Couet, *PAW tutorial*, <http://paw.web.cern.ch/paw/tutorial/>, CERN, Geneva, Switzerland, 1999.
- [46] O. Couet, *PAW – Physics Analysis Workstation, User's guide*, <http://wwwasdoc.web.cern.ch/wwwasdoc/psdir/paw.ps.gz>, CERN, Geneva, Switzerland, 2000.
- [47] Yu. Shitov, K. Errahmane, X. Sarazin, and L. Simard (NEMO Collaboration), *Description of the pre-analysis and visualisation programs developed at LAL*, internal NEMO note, LAL Orsay, 2001.
- [48] L. Simard (NEMO Collaboration), private communication.

- [49] Yu. Shitov and V. Tretyak (NEMO Collaboration), *NEMO database – Users and programmers guide*, internal NEMO note, 2002.
- [50] NEMO3 data base, <http://ireswww.in2p3.fr/ires/recherche/nemo/db/>, IReS, Strasbourg, 2004.
- [51] L. Vála (NEMO Collaboration), private communication.